

This article may be downloaded for personal use only. Any other use requires prior permission of the author and AIP Publishing. This article appeared in:

Journal of Applied Physics **124**, 154302 (2018)

and may be found at:

<https://doi.org/10.1063/1.5052236>

Size-dependent effects sensitively determine buckling of a cylindrical silicon electrode particle in a lithium-ion battery

Srijan Neogi and Jeevanjyoti Chakraborty^{a)}

Mechanical Engineering Department, Indian Institute of Technology Kharagpur, Kharagpur 721302, West Bengal, India

(Received 15 August 2018; accepted 27 September 2018; published online 17 October 2018)

The influence of size-dependent effects on mechanical behavior of a cylindrical silicon electrode particle within a lithium-ion battery is investigated, and it is shown that these effects sensitively determine critical buckling behavior. The mathematical framework used for this investigation incorporates the bond-order-length-strength (BOLS) theory correlation in a general finite deformation theory model that includes the two-way coupling between diffusion-induced stress and stress-influenced diffusion. Additionally, the possibility of plastic flow is accounted for in the model to allow probing situations with relatively high charging rates. Significant differences, arising due to the consideration of the size-dependent effects and captured through the BOLS theory, are highlighted. In particular, it is found that, in most cases studied, both stresses and plastic stretches are amplified in magnitude. Tensile to compressive stress reversal also takes place faster on considering the BOLS theory. The modeling framework is further applied to estimate critical lengths that are safe against buckling. Thus, it is expected that the presented framework will provide an improved aid for the design of nanowire-based lithium ion battery silicon electrodes. *Published by AIP Publishing.*

<https://doi.org/10.1063/1.5052236>

I. INTRODUCTION

The demand for a fast-charging, longer-lasting, and higher power density battery source in a lighter package has led to tremendous efforts in developing lithium-ion battery technology. Such developments have established lithium-ion batteries as the preferred energy storage medium for portable electronic devices like laptops, mobile phones, and cameras. They are also the power source of choice for modern hybrid electric vehicles (HEV), plug-in HEV (PHEV), and electric vehicles (EV). Lithium is the lightest metal and Li-ion batteries have a higher energy density than conventional batteries.¹ However, Li-ion batteries having much higher energy density are required so as to extend their use in large-scale applications. This requires consideration of new materials. One such promising new material is silicon (Si) for the anode. The motivation for work on Si-based anodes is four-fold. First and foremost, in the amorphous phase of $\text{Li}_{22}\text{Si}_5$, each atom of Si can accommodate up to 4.4 Li atoms² and thus has a very high theoretical specific capacity of 4200 mAh g^{-1} , whereas when graphite is used as the anode, LiC_6 is obtained in the fully lithiated state which has a significantly lower specific capacity of 372 mAh g^{-1} . Secondly, silicon is inexpensive and non-toxic. The third reason is the safety concern associated with the risk of high-surface-area Li decomposition encountered with graphite anode at the end of fast recharge.¹ A slightly higher (than Li^0/Li^+ redox potential) onset voltage potential in case of Si anode eliminates this safety issue.³ Finally, synthesis methods of Si

nanoparticles are quite advanced and Si nano-particles are commercially available.⁴

Commercial use of Si in the battery industry is currently hindered due to the large lithiation-induced volume changes in Si which can go up to 320% for the fully lithiated state.⁵⁻⁹ This volume expansion is due to the ability of Si to accommodate high amounts of Li. This large variation in volume gives rise to stresses within the silicon due to inhomogeneous Li concentration and externally imposed geometric constraints. Upon cyclic charging/discharging, these stresses may result in mechanical failure of the Si anode particles and a drastic change in the specific capacity¹⁰⁻¹² and also lead to the situation in which some of the anode particles are disconnected from the conductive carbon and from the current collector.¹³⁻¹⁵ This problem of inhomogeneous swelling and resulting stresses can be solved by the use of smaller Si particle as only nano-structured electrodes can endure the strains due to the change of volume and avoid cracking.^{11,16-19} The large surface-to-volume ratio of nano-scale structures like nanowires and nanotubes allows stress relaxation and increases flaw tolerance; hence, they are tougher than their bulk counterpart.²⁰ The reduction of diffusion path length of both electron and lithium which enhances the rate of chemical reactions is another motivation for the reduction of size to nanoscale.²⁰⁻²²

It has been established by Chan *et al.*¹¹ that compared to particles with a spherical or thin film geometry, particles with a cylindrical geometry, such as in nanowires or nanopillars, are much less susceptible to cracking even though they undergo increases in diameter and length. Cracking, however, is just one form of mechanical failure. It is possible that slender structures as nanowires or nanopillars on increasing in length (due to lithiation) may press against the rigid narrow confinements of a battery and may fail through

^{a)}Electronic addresses: jeevan@mech.iitkgp.emet.in and jeevanjyoti4@gmail.com

buckling. Indeed, it was shown by Chan *et al.*¹¹ that when free axial growth is constrained by a rigid backbone in the form of thin nickel coating, the nanowire buckled into a helical shape. The possibility of such buckling has also been confirmed through molecular dynamics simulations.²³ At the whole electrode level, for an anode composed of a dense mesh of such silicon nanopillars, as fabricated by Ogata *et al.*,²⁴ the detrimental consequences of such buckling failures may be far-reaching.

Recognizing the wide-spread interest in the nanowire electrode architecture that goes beyond just silicon,²⁵ this failure mode has been recently modeled mathematically by Chakraborty *et al.*²⁶ to develop a better understanding and a framework for design. This mathematical model considered only radial diffusion of lithium and it was later extended to study, additionally, axial diffusion by Zhang *et al.*²⁷ The pioneering modeling work related to buckling in the context of lithium-ion batteries was carried out by Bhandakkar and Johnson,²⁸ albeit their interest was in a honeycomb architecture of the electrode.

Another important facet associated with the nanowire geometry is the significant dependence of the physical and mechanical properties on the size of the nanowire itself, specifically, its diameter. This behavior is in marked contrast to what is observed at macroscale dimensions. Pertinently, the canonical mechanical property of Young's modulus at macroscale dimensions depends only on the material, whereas at the nanoscale, the Young's modulus is not only material-dependent but is also dependent on the specimen size. In the particular context of lithium-ion batteries, size dependence has been shown to influence the surface stresses²⁹ and fracture^{30,31} in nanostructured electrode particles. The size dependence is attributed to the increasing importance of surface effects due to increasing surface area to volume ratio with decrease in size of the specimen. More fundamentally, a physical reason underlying a wide-spectrum of the size-dependent trends in a variety of contexts may be given in a unified manner based on the bond-order-length-strength (BOLS) theory.³² This theory is predicated on the understanding that, at the surface, the atoms have a coordination number imperfection which results in bond relaxation to minimize the system energy with consequent strengthening of the bonds. An important feature of this theory is that, while its origin is atomistic, it is nevertheless amenable to incorporation in a continuum setting via the BOLS correlation. Indeed, in a very recent work by Ma *et al.*,³³ the BOLS correlation was combined with a simple model of diffusion induced-stress in a lithium-ion battery electrode particle to show changes in the evolution of stress with different spherical particle diameters.

In light of these recent modeling developments into buckling as an important mode of mechanical failure of silicon anode particles and of size-dependent mechanical effects in nanoparticles, it is only natural to be curious about the question: *What, if any, is the influence of size-dependent effects on the buckling mode of failure of a silicon nanowire electrode particle?*

In this work, we investigate this question and show theoretically that size-dependent effects do become important for

nanowires of sufficiently small diameters and substantially influence critical buckling behavior. Our mathematical model incorporates the BOLS theory correlation within the generic framework presented by Chakraborty *et al.*²⁶ Here, we consider a two-way coupling between stress and concentration of Li in Si. Thus, we account for not only the effects of diffusion-induced stress, which has been thoroughly investigated over the years as well as recently,^{34–39} but also stress-influenced diffusion. This two-way coupling is enshrined within a finite deformation theory.⁴⁰ Additionally, we incorporate the possibility of plastic flow which allows us to probe situations with high charging rates. Furthermore, while computing the stresses, we have allowed for the Young's modulus to be varying radially being dependent on the inhomogeneous concentration. Thus, expanding the initial ideas of Ma *et al.*,³³ we aim to provide a more complete and refined mathematical model of the lithiation process of Si nanoelectrode particles. We also apply this model to study buckling behavior and provide estimates for critical lengths. Our framework is thus expected to provide an improved aid for the design of nanowire-based electrode architecture.

The rest of the paper is as follows. First, we present the mathematical formulation in Sec. II considering the general case (Sec. II A) of deformation of a cylindrical Si anode particle undergoing lithiation. In Sec. II B, we present the BOLS effect induced modification in Young's modulus. In Sec. II D, we include the size effect in the formula for flexural rigidity. In Sec. III, we present the result and discussion of our study focusing on the differences in calculated stresses in two cases—one in which BOLS effect is considered and one in which it is not. Finally, in Sec. III C, we discuss the differences in critical length of buckling that has been computed for the two cases.

II. MATHEMATICAL FORMULATION

We consider a single cylindrical silicon nano-anode particle which undergoes deformation during intercalation and deintercalation of lithium. We assume that both processes take place uniformly and axisymmetrically over the curved peripheral surface of the cylinder. We also assume that no surface reconstruction takes place which may give rise to dangling bonds at the surface. Following Chakraborty *et al.*,²⁶ we construct a model for axisymmetric deformation and consider two cases in which the cylinder is (i) unconstrained and (ii) physically constrained against deformation in the axial direction. The latter case provides an opportunity to investigate the possibility of mechanical failure of the anode through buckling.

A. General case

1. Deformation gradient decomposition

Let $\mathbf{X} \in \mathbb{A}$ be the initial position and $\mathbf{x} \in \mathbb{B}$ be the current position of a material point in the electrode particle, where \mathbb{A} and \mathbb{B} are the reference and deformed configurations of the electrode particle, respectively. The displacement field vector is given by

$$\mathbf{u}(\mathbf{X}) = \mathbf{x} - \mathbf{X}. \quad (1)$$

Since the geometry of the electrode particle is cylindrical, we use standard cylindrical coordinates (r, θ, z) in \mathbb{A} . The displacement field vector can be expressed as $\mathbf{u} = u\mathbf{e}_r + v\mathbf{e}_\theta + w\mathbf{e}_z \equiv [u \ 0 \ w]^T$, where due to our assumption of uniform axisymmetric behavior on the cylindrical surface, we take $v = 0$ to denote zero intrinsic displacement in the θ -direction. Similarly, we preclude any variation along the z -direction and assume that displacement, w , in the z -direction will not vary radially. Thus, the deformation gradient, defined as $\mathbf{F} = \text{Grad } \mathbf{u}$ reduces to the diagonal form

$$\mathbf{F} = \text{diag} \left(1 + \frac{\partial u}{\partial r}, 1 + \frac{u}{r}, 1 + \frac{\partial w}{\partial z} \right). \quad (2)$$

We should note that deformation is the total result of various mechano-chemical processes that occur during lithiation or delithiation. To take into account various processes, we follow the usual practice of decomposing the deformation gradient into three parts: (a) a reversible elastic part, (b) an expansion due to volume change as a consequence of lithiation, and (c) an irreversible plastic part which is volume-preserving. We carry out the decomposition in terms of total deformation gradient. The method of decomposing in terms of total deformation gradient instead of strain or total stretch was first proposed by Lee⁴¹ and is widely used in finite deformation modeling in lithium-ion batteries.^{26,40} We have

$$\mathbf{F} = \mathbf{F}^p \mathbf{F}^e \mathbf{F}^{\text{SF}}, \quad (3)$$

where \mathbf{F}^e is elastic deformation gradient, \mathbf{F}^{SF} is stress-free volumetric deformation gradient, and \mathbf{F}^p is plastic deformation gradient.

In the absence of anisotropy, the order in which deformation gradient constituent appears in Eq. (3) is irrelevant. Gao *et al.*⁴² have provided a physical interpretation of this decomposition in the context of batteries. In this decomposition, the deformation gradient \mathbf{F}^{SF} is due to the unconstrained shape change associated with intercalation or deintercalation and so it is denoted as “stress-free.” Assuming the volumetric change is isotropic, the stress free deformation gradient becomes

$$\mathbf{F}^{\text{SF}} = (J^c)^{1/3} \mathbf{I}, \quad (4)$$

$$J^c = 1 + 3\eta x_{\text{max}} c, \quad (5)$$

where η is the coefficient of compositional expansion, x is the number of moles of Li per mole of Si, $x_{\text{max}} = 4.4$ (the maximum value of x), and $c = x/x_{\text{max}}$ (non-dimensional measure of Li concentration).

Simply put, x denotes the saturation of Li in Li_xSi . The justification for assuming isotropic material properties has been explained by Chakraborty *et al.*²⁶ When the concentration c is uniform, \mathbf{F}^{SF} will not create any residual stress as \mathbf{F}^{SF} is a multiple of the identity. The deformation gradient \mathbf{F}^p is volume-preserving and hence we have $\det(\mathbf{F}^p) = 1$. We consider $\mathbf{F}^p = \text{diag}(\lambda_r, \lambda_\theta, \lambda_z)$ and so

$$\det(\mathbf{F}^p) = \det[\text{diag}(\lambda_r, \lambda_\theta, \lambda_z)] = \lambda_r \lambda_\theta \lambda_z = 1. \quad (6)$$

Therefore, the elastic part of the deformation gradient becomes

$$\begin{aligned} \mathbf{F}^e &= \mathbf{F}(\mathbf{F}^p)^{-1}(\mathbf{F}^{\text{SF}})^{-1} \\ &= (J^c)^{-1/3} \text{diag} \left(\frac{1 + \partial u / \partial r}{\lambda_r}, \frac{1 + u/r}{\lambda_\theta}, \frac{1 + \partial w / \partial z}{\lambda_z} \right). \end{aligned} \quad (7)$$

For the elastic strain, we have

$$\mathbf{E}^e = \frac{1}{2} [(\mathbf{F}^e)^T \mathbf{F}^e - \mathbf{I}] = \text{diag}(E_r^e, E_\theta^e, E_z^e), \quad (8)$$

where the components can be written as

$$E_r^e = \frac{1}{2} [(F_r^e)^2 - 1] = \frac{1}{2} (J^c)^{-2/3} \frac{(1 + \partial u / \partial r)^2}{\lambda_r^2} - \frac{1}{2}, \quad (9a)$$

$$E_\theta^e = \frac{1}{2} [(F_\theta^e)^2 - 1] = \frac{1}{2} (J^c)^{-2/3} \frac{(1 + u/r)^2}{\lambda_\theta^2} - \frac{1}{2}, \quad (9b)$$

$$E_z^e = \frac{1}{2} [(F_z^e)^2 - 1] = \frac{1}{2} (J^c)^{-2/3} \frac{(1 + \partial w / \partial z)^2}{\lambda_z^2} - \frac{1}{2}. \quad (9c)$$

2. Elastic deformation

We will reasonably assume that during deformation the elastic strains remain small enough so that we can use a strain-energy density function in the reference frame of the form²⁶

$$\begin{aligned} W &= \frac{J^c Y(c, \chi_s)}{2(1+\nu)} \left[\frac{\nu}{1-2\nu} (E_{kk}^e)^2 + E_{jk}^e E_{kj}^e \right] \\ &= \frac{J^c Y(c, \chi_s)}{2(1+\nu)} \left[\frac{\nu}{1-2\nu} \{E_r^e + E_\theta^e + E_z^e\}^2 \right. \\ &\quad \left. + (E_r^e)^2 + (E_\theta^e)^2 + (E_z^e)^2 \right], \end{aligned} \quad (10)$$

where Young's modulus, $Y(c, \chi_s)$, is a function of concentration “ c ” and the BOLS effect parameter “ χ_s ,” which is discussed in detail in Sec. II B and ν is the Poisson's ratio. Note that E_r^e, E_θ^e, E_z^e are the strain components. Thus, the first Piola-Kirchhoff stress, $\mathbf{P} = \text{diag}(\sigma_r^0, \sigma_\theta^0, \sigma_z^0)$, is given by

$$\begin{aligned} \sigma_r^0 &= \frac{1}{F_r^*} \frac{\partial W}{\partial F_r^e} \\ &= J^c \frac{Y(c, \chi_s)}{(1+\nu)(1-2\nu)} \left[(1-\nu)E_r^e + \nu(E_\theta^e + E_z^e) \right] \frac{2E_r^e + 1}{1 + \partial u / \partial r}, \end{aligned} \quad (11a)$$

$$\begin{aligned}\sigma_{\theta}^0 &= \frac{1}{F_{\theta}^*} \frac{\partial W}{\partial F_{\theta}^e} \\ &= J^c \frac{Y(c, \chi_s)}{(1+\nu)(1-2\nu)} \left[(1-\nu)E_{\theta}^e + \nu(E_z^e + E_r^e) \right] \frac{2E_{\theta}^e + 1}{1+u/r},\end{aligned}\quad (11b)$$

$$\begin{aligned}\sigma_z^0 &= \frac{1}{F_z^*} \frac{\partial W}{\partial F_z^e} \\ &= J^c \frac{Y(c, \chi_s)}{(1+\nu)(1-2\nu)} \left[(1-\nu)E_z^e + \nu(E_r^e + E_{\theta}^e) \right] \frac{2E_z^e + 1}{1+\partial w/\partial z},\end{aligned}\quad (11c)$$

where $\text{diag}(F_r^*, F_{\theta}^*, F_z^*) = \mathbf{F}^p \mathbf{F}^{SF} = (J^c)^{1/3} \text{diag}(\lambda_r, \lambda_{\theta}, \lambda_z)$. For mechanical equilibrium $\text{Div } \mathbf{P} = 0$, from which we obtain

$$\frac{\partial \sigma_r^0}{\partial r} + \frac{\sigma_r^0 - \sigma_{\theta}^0}{r} = 0. \quad (12)$$

Dependence of the Cauchy stresses $\boldsymbol{\sigma} = \text{diag}(\sigma_r, \sigma_{\theta}, \sigma_z)$ on the Piola-Kirchhoff stress is given by $\boldsymbol{\sigma} = J^{-1} \mathbf{P} \mathbf{F}^T$ so that

$$\begin{aligned}\sigma_r &= \frac{Y(c, \chi_s)}{(1+\nu)(1-2\nu)} \left[(1-\nu)E_r^e + \nu(E_{\theta}^e + E_z^e) \right] \\ &\quad \times \frac{\sqrt{2E_r^e + 1}}{\sqrt{2E_{\theta}^e + 1} \sqrt{2E_z^e + 1}},\end{aligned}\quad (13a)$$

$$\begin{aligned}\sigma_{\theta} &= \frac{Y(c, \chi_s)}{(1+\nu)(1-2\nu)} \left[(1-\nu)E_{\theta}^e + \nu(E_z^e + E_r^e) \right] \\ &\quad \times \frac{\sqrt{2E_{\theta}^e + 1}}{\sqrt{2E_z^e + 1} \sqrt{2E_r^e + 1}},\end{aligned}\quad (13b)$$

$$\begin{aligned}\sigma_z &= \frac{Y(c, \chi_s)}{(1+\nu)(1-2\nu)} \left[(1-\nu)E_z^e + \nu(E_r^e + E_{\theta}^e) \right] \\ &\quad \times \frac{\sqrt{2E_z^e + 1}}{\sqrt{2E_r^e + 1} \sqrt{2E_{\theta}^e + 1}}.\end{aligned}\quad (13c)$$

3. Plastic flow

The rate of plastic deformation gradient \mathbf{D}^p is given by

$$\mathbf{D}^p = \dot{\mathbf{F}}^p (\mathbf{F}^p)^{-1} = \text{diag} \left(\frac{\dot{\lambda}_r}{\lambda_r}, \frac{\dot{\lambda}_{\theta}}{\lambda_{\theta}}, \frac{\dot{\lambda}_z}{\lambda_z} \right), \quad (14)$$

where a dot represents the time derivative in the reference frame. The viscoplastic behavior of lithiated silicon can be described by the constitutive equation

$$\mathbf{D}^p = \frac{\partial G(\boldsymbol{\sigma}_{\text{eff}})}{\partial \boldsymbol{\tau}}, \quad (15)$$

where $\boldsymbol{\tau} = \boldsymbol{\sigma} - \frac{1}{3} \text{tr}(\boldsymbol{\sigma}) \mathbf{I}$ is the deviatoric part of the Cauchy

stress, the effective stress is given by

$$\sigma_{\text{eff}} = \sqrt{\frac{3}{2}} \sqrt{\boldsymbol{\tau} : \boldsymbol{\tau}} = \sqrt{\frac{3}{2}} \sqrt{\tau_r^2 + \tau_{\theta}^2 + \tau_z^2} \quad (16)$$

and G is the flow potential given as

$$G(\boldsymbol{\sigma}_{\text{eff}}) = \frac{\sigma_f \dot{d}_0}{m_p + 1} \left(\frac{\sigma_{\text{eff}}}{\sigma_f} - 1 \right)^{m_p + 1} H \left(\frac{\sigma_{\text{eff}}}{\sigma_f} \right), \quad (17)$$

where σ_f is the initial yield stress of Si, \dot{d}_0 is the characteristic strain rate for plastic flow in Si, m_p is the stress exponent for plastic flow in Si, and $H \left(\frac{\sigma_{\text{eff}}}{\sigma_f} \right)$ is the unit step function

$$= \begin{cases} 0, & \text{if } \frac{\sigma_{\text{eff}}}{\sigma_f} < 1 \text{ and } 1, & \text{if } \frac{\sigma_{\text{eff}}}{\sigma_f} \geq 1. \end{cases}$$

Hence, we obtain the three plastic stretches as solutions of

$$\frac{\dot{\lambda}_r}{\lambda_r} = \sqrt{\frac{3}{2}} \dot{d}_0 \left(\frac{\sigma_{\text{eff}}}{\sigma_f} - 1 \right)^m \frac{\tau_r}{\sqrt{\tau_r^2 + \tau_{\theta}^2 + \tau_z^2}} H \left(\frac{\sigma_{\text{eff}}}{\sigma_f} \right), \quad (18a)$$

$$\frac{\dot{\lambda}_{\theta}}{\lambda_{\theta}} = \sqrt{\frac{3}{2}} \dot{d}_0 \left(\frac{\sigma_{\text{eff}}}{\sigma_f} - 1 \right)^m \frac{\tau_{\theta}}{\sqrt{\tau_r^2 + \tau_{\theta}^2 + \tau_z^2}} H \left(\frac{\sigma_{\text{eff}}}{\sigma_f} \right), \quad (18b)$$

$$\frac{\dot{\lambda}_z}{\lambda_z} = \sqrt{\frac{3}{2}} \dot{d}_0 \left(\frac{\sigma_{\text{eff}}}{\sigma_f} - 1 \right)^m \frac{\tau_z}{\sqrt{\tau_r^2 + \tau_{\theta}^2 + \tau_z^2}} H \left(\frac{\sigma_{\text{eff}}}{\sigma_f} \right). \quad (18c)$$

It is to be noted that the three equations are all not independent as $\lambda_r \lambda_{\theta} \lambda_z = 1$ and so

$$\frac{\dot{\lambda}_r}{\lambda_r} + \frac{\dot{\lambda}_{\theta}}{\lambda_{\theta}} + \frac{\dot{\lambda}_z}{\lambda_z} = 0, \quad (19)$$

which is consistent with $\text{tr}(\boldsymbol{\tau}) = 0$.

4. Lithium diffusion

The conservation equation for the concentration field is given by

$$\frac{1}{V_m^{\text{Si}}} \frac{\partial c}{\partial t} = -\frac{1}{r} \frac{\partial (rJ_r)}{\partial r}, \quad (20)$$

where

V_m^{Si} = molar volume of Si,

J_r = the flux of Li (not to be confused with J^c)

$$= -\frac{D}{R_g T} \frac{c}{V_m^{\text{Si}}} \frac{\partial \mu}{\partial r}, \quad (21)$$

D = diffusivity of Li in Si,

R_g = Universal gas constant,

T = temperature.

The chemical potential, μ , of the lithiated silicon can be

decomposed as

$$\mu = \mu_0 + \mu_s, \quad (22)$$

where μ_0 is stress independent and μ_s is stress dependent. The stress-independent part is written as

$$\mu_0 = \mu_0^0 + R_g T \log(\gamma c), \quad (23)$$

where μ_0^0 , a constant, represents the chemical potential at a standard state and γ is the activity coefficient representing the effects of interactions among the atoms or molecules which leads to non-ideal behavior. Furthermore, the stress dependent part can be expressed as

$$\begin{aligned} \mu_s &= \frac{V_m^{\text{Si}}}{x_{\text{max}}} \left[-\frac{1}{3} \frac{\partial J^c}{\partial c} F_{im}^e F_{in}^e C_{mnlk} E_{kl}^e \right. \\ &\quad \left. + \frac{1}{2} \left(J^c \frac{\partial C_{ijkl}}{\partial c} + \frac{\partial J^c}{\partial c} C_{ijkl} \right) E_{ij}^e E_{kl}^e \right] \\ &= \frac{V_m^{\text{Si}}}{x_{\text{max}}} \left[-\frac{1}{3} \frac{\partial J^c}{\partial c} \{ (\mathbf{F}^e)^T \mathbf{F}^e \} : \sigma^{0e} \right. \\ &\quad \left. + \frac{1}{2} J^c \frac{\partial C_{ijkl}}{\partial c} E_{ij}^e E_{kl}^e + \frac{1}{2} \frac{\partial J^c}{\partial c} \mathbf{E}^e : \sigma^{0e} \right] \\ &= \frac{V_m^{\text{Si}}}{x_{\text{max}}} \left[-\frac{1}{6} \frac{\partial J^c}{\partial c} \mathbf{E}^e : \sigma^{0e} - \frac{1}{3} \text{tr}(\sigma^{0e}) \frac{\partial J^c}{\partial c} \right. \\ &\quad \left. + \frac{1}{2} J^c \frac{\partial C_{ijkl}}{\partial c} E_{ij}^e E_{kl}^e \right], \end{aligned} \quad (24)$$

where C is the concentration-dependent fourth-rank stiffness tensor. Here, we have used the equality $\mathbf{F}_e^T \mathbf{F}_e = 2\mathbf{E}_e + \mathbf{I}$. The three terms of Eq. (24) can be simplified because

$$\begin{aligned} -\frac{1}{6} \frac{\partial J^c}{\partial c} \mathbf{E}^e : \sigma^{0e} &= -\frac{1}{6} \frac{\partial J^c}{\partial c} \frac{Y(c, \chi_s)}{(1+\nu)(1-2\nu)} \\ &\quad \times \left[(1-\nu) \{ (E_r^e)^2 + (E_\theta^e)^2 + (E_z^e)^2 \} \right. \\ &\quad \left. + 2\nu (E_r^e E_\theta^e + E_\theta^e E_z^e + E_z^e E_r^e) \right], \end{aligned} \quad (25a)$$

$$\begin{aligned} \frac{1}{3} \text{tr}(\sigma^{0e}) \frac{\partial J^c}{\partial c} &= -\frac{1}{3} \frac{\partial J^c}{\partial c} \frac{Y(c, \chi_s)}{(1+\nu)(1-2\nu)} \\ &\quad \times \left[(1-\nu) \{ E_r^e + E_\theta^e + E_z^e \} \right. \\ &\quad \left. + 2\nu (E_r^e + E_\theta^e + E_z^e) \right], \end{aligned} \quad (25b)$$

$$\begin{aligned} \frac{1}{2} J^c \frac{\partial C_{ijkl}}{\partial c} E_{ij}^e E_{kl}^e &= \frac{1}{2} J^c \left[\frac{\partial}{\partial c} \left\{ \frac{Y(c, \chi_s)}{(1+\nu)(1-2\nu)} \right\} \right. \\ &\quad \times \left\{ (E_r^e)^2 + (E_\theta^e)^2 + (E_z^e)^2 \right\} \\ &\quad \left. + 2 \frac{\partial}{\partial c} \left\{ \frac{Y(c, \chi_s)\nu}{(1+\nu)(1-2\nu)} \right\} \right. \\ &\quad \left. \times (E_r^e E_\theta^e + E_\theta^e E_z^e + E_z^e E_r^e) \right]. \end{aligned} \quad (25c)$$

The activity, γ , and diffusivity, D , will be taken to have the empirically determined forms,

$$\begin{aligned} \gamma &= \frac{1}{1-c} \exp \left[\frac{1}{R_g T} \{ 2(A_0 - 2B_0)c - 3(A_0 - B_0)c^2 \} \right], \\ D &= D_0 \exp \left(\frac{\alpha V_m^B \sigma_\theta^0}{R_g T} \right), \end{aligned} \quad (26)$$

where the parameters A_0 , B_0 , α and the concentration-independent coefficient of the diffusivity D_0 are given in Table I.

5. Initial and boundary conditions

As an initial condition, we take a pristine, stress-free, Li-free nano-electrode particle, that is,

$$\lambda_r(r, 0) = \lambda_\theta(r, 0) = 1, \quad u(r, 0) = 0, \quad c(r, 0) = 0. \quad (27)$$

The curved surface of the cylinder, $r = R_0$, is assumed to be free from physical constraints. Thus, we can impose a

TABLE I. Values of parameters and material properties.

Parameter or material property	Value
A_0 , parameter used in γ	$-29\,549 \text{ J mol}^{-1a}$
B_0 , parameter used in γ	$-38\,618 \text{ J mol}^{-1a}$
D_0 , diffusivity of Si	$1 \times 10^{-16} \text{ m}^2 \text{ s}^{-1b}$
\dot{d}_0 , plastic flow strain rate in Si	$1 \times 10^{-3} \text{ s}^a$
Y_0 , modulus of elasticity of pure Si	90.13 GPa^a
m_p , stress exponent for plastic flow in Si	4^c
R_g , universal gas constant	$8.314 \text{ J K}^{-1} \text{ mol}^{-1}$
T , temperature	300 K
V_m^{Si} , molar volume of Si	$1.2052 \times 10^{-5} \text{ m}^3 \text{ mol}^{-1a}$
x_{max} , maximum concentration of Li in Si	4.4
α , coefficient of diffusivity	0.18^a
η , coefficient of compositional expansion	0.2356^a
η_{E_s} , rate of change of modulus of elasticity with concentration	-0.1464^a
ν , Poisson's ratio of Si	0.28^a
σ_f , initial yield stress of Si	0.12 GPa^d

^aReference 40.

^bReference 43.

^cReference 44.

^dReference 45.

traction-free boundary condition at the surface as

$$\sigma_r^0(R_0, t) = 0. \quad (28)$$

Since the cylinder as a whole is immobile, we apply a no displacement condition at the centre

$$u(0, t) = 0. \quad (29)$$

The boundary condition at the surface for the concentration can be expressed by relating the flux to the linearised version of the Butler-Volmer condition as

$$J_r = J_0(1 - c), \quad (30)$$

while at the centre of the cylinder, we have

$$J_r = 0. \quad (31)$$

Regarding the top and the bottom faces of the cylinder, we consider two cases. In the first case, we consider the ends to be free from any physical constraints. We refer to this case as the axially unconstrained case. Since, there is no net force in the axial direction, the condition translates to

$$\int_0^{R_0} \sigma_z^0 dA = 2\pi \int_0^{R_0} \sigma_z^0 r dr = 0. \quad (32)$$

In the second case, we prevent the deformation of the ends of the cylinder in the axial direction by imposing physical constraints. We refer to this case as the axially constrained case. It is assumed that such a physical constraint can be imposed without restraining the lateral movement of the ends of the cylinder. Thus, in this case, we impose a boundary condition at the ends as $\partial w / \partial z = 0$.

B. Bond-order-length-strength (BOLS) theory and modification of Young's modulus

According to the BOLS theory, bond breaking gives rise to a spontaneous contraction of the bonds of under-coordinated atoms unless the process is proceeding under external stimuli such as heating or pressure. If the coordination number of an atom is reduced, its metallic and ionic radius also decreases spontaneously. The coordination number induced bond reduction is universal in the sense that it is independent of nature of chemical bond, structural phases, or type of element.⁴⁶⁻⁴⁸ As the bond length is reduced, bond strength will increase and the system energy will be lowered.⁴⁹ Therefore, the BOLS induced bond relaxation can be defined as $d_i = C_i d_b$ by introducing a non-dimensional coefficient $C_i < 1$ for bond contraction and $C_i > 1$ for bond relaxation.³² Bond contraction and the corresponding change in bond energy is expressed as³²

$$\frac{\Delta d_i}{d_b} = C_i - 1 < 0, \quad (33)$$

$$\frac{\Delta E_b(d_i)}{E_b(d_b)} = C_i^{-m} - 1, \quad (34)$$

where C_i is coefficient of bond contraction, d is bond length, and E_b is binding energy. The subscript b and i denote an atom in the bulk and i th atomic layer counted from the outermost surface to the centre of the solid. m describes the bond length dependence of the change in binding energy and is determined from experiments.⁵⁰ The function $C_i(z_i)$ is established so that it fits the observations of Goldschmidt⁵¹ and Fiebelman⁵² with the aim to reduce the number of freely adjustable parameters.³² The BOLS correlation mechanism can be formulated as a consequence of the atomic ‘‘coordination-radius’’ theorised by Pauling and Goldschmidt^{53,51} as⁵⁰

$$\begin{cases} C_i = \frac{d_i}{d_b} = \frac{2}{1 + \exp[(12 - z_i)/(8z_i)]} & \text{(BOLS-coefficient),} \\ E_b(d_i) = C_i^{-m} E_b(d_b) & \text{(Single-bond-energy),} \\ E_{Bi} = z_i E_i & \text{(Atomic-coherency),} \end{cases} \quad (35)$$

where E_{Bi} is atomic cohesive energy of an atom in the i th atomic layer and z_i is effective coordination number of the i th atom.

No coordination-number reduction is expected for $i > 3$ and hence i is only counted up to three from the outermost atomic layer toward centre of the solid.^{49,54} The index m indicates the nature of bond in a particular material. For silicon, the accepted value of m is 4.88.³² z_i depends on the size and curvature of a nanostructure and is determined by

$$\begin{cases} z_1 = \begin{cases} 4(1 - 0.7/K) & \text{(Curved-surface),} \\ 4 & \text{(Flat-surface),} \end{cases} \\ z_2 = z_1 + 2, \\ z_3 = 12, \end{cases} \quad (36)$$

where $K = R/d_0$ is the number of atoms along the radius of the nanowire, R is current radius of the silicon nanowire, and d_0 is the average bond length ($= 0.278$ nm).

The volume or number ratio of a certain atomic layer, i , to that of the entire solid is expressed as³²

$$\gamma_i = \frac{N_i}{N} = \frac{V_i}{V} = \frac{\tau[K - (i - 0.5)]^{\tau-1}}{K^\tau - L^\tau} C_i = \gamma_{i0} c_i \ll 1, \quad (37)$$

τ is the dimensionality. For a thin plate, $\tau = 1$, for a cylindrical rod, $\tau = 2$, and for a sphere, $\tau = 3$. L is the number of atomic layers not occupied by atoms. Since the nanoparticle under consideration is a solid, $L=0$ in our study. Further, i is of the order of 1 ($i \leq 3$) and $K = R/d_0$ is at least of the order of 10 (minimum value of $K=17.98$, in our study). Therefore, γ_i can be further simplified into

$$\gamma_i = \frac{\tau[K - (i - 0.5)]^{\tau-1}}{K^2 - 0^2} C_i \approx \frac{\tau K}{K^2} C_i = \frac{\tau}{K} C_i. \quad (38)$$

Let the mean Young's modulus Y of a nanosolid with N atoms having dimension D be expressed as $Y(D)$, while denoting the same solid without considering the BOLS effect

as $Y(\infty)$. Let y and y_s correspond to the density of Y in the bulk and the surface, respectively. Thus,

$$Y(\infty) = Ny, \quad (39)$$

$$Y(D) = (N - N_s)y + N_s y_s = Ny + N_s(y_s - y), \quad (40)$$

where $N_s = \sum N_i$ is the number of atom on the surface atomic shell. Therefore,

$$\begin{aligned} \frac{\Delta Y(D)}{Y(\infty)} &= \frac{Y(D) - Y(\infty)}{Y(\infty)} = \frac{[Ny + N_s(y_s - y)] - (Ny)}{Ny} \\ &= \frac{N_s(y_s - y)}{Ny} = \frac{N_s}{N} \left(\frac{y_s}{y} - 1 \right) = \frac{\sum_{i \leq 3} N_i (y_i - y)}{Ny} \\ &= \sum_{i \leq 3} \frac{N_i}{N} \left(\frac{y_i}{y} - 1 \right) = \sum_{i \leq 3} \gamma_i \left(\frac{y_i}{y} - 1 \right) \\ &= \sum_{i \leq 3} \frac{\tau}{K} C_i \left(\frac{y_i}{y} - 1 \right) = \sum_{i \leq 3} \frac{\tau d_0}{R} C_i \left(\frac{y_i}{y} - 1 \right). \end{aligned} \quad (41)$$

Surface stress connects microscopic bonding to the macroscopic properties and plays a crucial role in the thermodynamics and acoustics of the surface.^{32,55,56} Let $u(r)$ be the binding energy at equilibrium atomic separation. The Young's modulus Y and the surface stress P at a surface can be expressed as functions of binding energy E_b , volume $v \propto d^3$, and atomic distance d as⁵⁷

$$P = - \left. \frac{\partial u}{\partial v} \right|_{r=d} \propto \frac{E_b}{d^3}, \quad (42)$$

$$Y = v \frac{\partial P}{\partial v} = -v \left. \frac{\partial^2 u}{\partial v^2} \right|_{r=d} \propto \frac{E_b}{d^3}. \quad (43)$$

Therefore, from Eqs. (35) and (43)

$$\frac{y_i}{y} = \frac{\frac{Y_i}{d_i^3}}{\frac{Y}{d_b^3}} = \frac{Y_i d_b^3}{Y d_i^3} = \frac{E_b(d_i) d_b^3}{E_b(d_b) d_i^3} = \frac{C_i^{-m}}{C_i^3} = C_i^{-(m+3)}. \quad (44)$$

Substituting Eq. (44) in (41), we can get a relationship between change in mean Young's modulus Y (dropping the dimensionality D) and C_i as³³

$$\frac{\Delta Y}{Y_\infty} = \frac{Y - Y_\infty}{Y_\infty} = \frac{\tau d_0}{R} \left[\sum_{i \leq 3} C_i \left(C_i^{-(m+3)} - 1 \right) \right] = \chi_s, \quad (45)$$

where ΔY is change in Young's modulus and $\tau = 2$ (corresponding to a cylindrical rod^{58,59}). Hence,

$$Y = Y_\infty (1 + \chi_s). \quad (46)$$

It is noteworthy that χ_s is the key dimensionless parameter that establishes the link between the BOLS theory and the continuum framework. The BOLS theory provides the fundamental understanding behind the increasing importance of surface layers as the size of the nanoparticle goes down.

However, it is through χ_s that changes in the Young's modulus (a macroscopic parameter) due to changes in size can be accounted for based on the BOLS theory. Specifically, χ_s can be physically interpreted as the change in Young's modulus relative to a constant, bulk value due to smaller size which, in turn, is fundamentally due to increasing importance of the surface layers. Importantly, for sufficiently large particles, χ_s tends to zero which means that there is practically no change in Young's modulus from the bulk value for such particles; that is, even though surface layers are present, their influence in changing the Young's modulus is negligible.

According to Chakraborty *et al.*,²⁶ Young's modulus is also dependent on concentration as

$$\begin{aligned} Y_\infty &= Y_0 (1 + \eta_{EX} x_{max} c) \\ &= Y_0 (1 + \chi_c). \end{aligned} \quad (47)$$

Here, χ_c can be viewed as the non-dimensional concentration effect factor. In terms of Eqs. (46) and (47) simultaneously, we can write

$$Y = Y_0 (1 + \chi_c) (1 + \chi_s). \quad (48)$$

We should note that the above method of deriving the Young's modulus due to the BOLS effect can be used to calculate the BOLS dependence of any other traditional macroscopic quantity Q which is dependent on the binding energy density in the relaxed region. The energy density determines the Hamiltonian and hence contributes to properties like bandgap, magnetization, surface stress, phonon frequency, and the Young's modulus.³²

It is important to note that the BOLS theory has not been fundamentally modified to account for Si-Si bond breaking and subsequent Si-Li bond formation as Li concentration increases, but we do incorporate the effect of increasing Li concentration into the Young's modulus (which is the specific way that the BOLS theory affects our continuum framework) through a softening parameter χ_c [see Eq. (48)]. Furthermore, we would like to point out that the effect of increasing concentration on the overall BOLS factor χ_s is taken into account in an indirect way through the use of the current value of the radius instead of the original radius. Pertinently, this increase in radius is a direct result of the increase in concentration. These effects have been duly incorporated in our calculations and results shown.

C. Non-dimensionalization of the variables

The non-dimensionalization is done by setting

$$\begin{aligned} \tilde{r} &= \frac{r}{R_0}, \quad \tilde{z} = \frac{z}{L_0}, \quad \tilde{t} = \frac{D_0}{R_0^2} t, \quad \tilde{u} = \frac{u}{R_0}, \quad \tilde{w} = \frac{w}{L_0}, \\ \tilde{J}_{r,0} &= \frac{V_m^B R_0}{D_0} J_{r,0}, \quad \tilde{\sigma}_{r,\theta,z,\text{eff},f} = \frac{V_m^B}{R_g T} \sigma_{r,\theta,z,\text{eff},f}, \quad \tilde{\mu}_{0,S} = \frac{1}{R_g T} \mu_{0,S}. \end{aligned} \quad (49)$$

The initial radius R_0 of a pristine, stress-free, Li-free electrode is taken as a length scale for both the radial coordinate, r , and the radial displacement field, u . Similarly, the initial length, L_0 , of the cylindrical electrode is taken as the length scale for both the axial coordinate, z , and the axial displacement field, w . R_0^2/D_0 , the time Li takes to diffuse a distance equal to the undeformed radius of the cylindrical Si anode particle has been used as a physically intuitive measure of time scale. The justification for the scale chosen for the influx rate is simple. The number of moles of Li diffused into the Si may be estimated using the concentration measure of Li, c , and the molar volume of Si, V_m^{Si} ; therefore, in terms of number of moles per unit length of the cylinder, the concentration scales as R_0^2/V_m^{Si} . The rate of influx is measured per unit time, per unit surface area and hence, for the flux scale, we need the surface area measure, R_0 (per unit length of the cylinder), and the already chosen time scale R_0^2/D_0 . Therefore, we obtain the flux scale as $(R_0^2/V_m^{\text{Si}})(1/R_0)(D_0/R_0^2)$, i.e., $D_0/(V_m^{\text{Si}}R_0)$. Non-dimensionalizing the governing equations, we obtain

$$\frac{\partial c}{\partial \tilde{t}} = -\frac{\partial \tilde{J}_r}{\partial \tilde{r}} - \frac{\tilde{J}_r}{\tilde{r}}, \quad (50)$$

$$\frac{\partial \tilde{\sigma}_r^0}{\partial \tilde{r}} + \frac{\tilde{\sigma}_r^0 - \tilde{\sigma}_\theta^0}{\tilde{r}} = 0, \quad (51)$$

$$\frac{\partial \lambda_r}{\partial \tilde{t}} = \sqrt{\frac{3}{2}} \lambda_r \dot{d}_0 \frac{R_0^2}{D_0} \left(\frac{\tilde{\sigma}_{\text{eff}}}{\tilde{\sigma}_f} - 1 \right)^{m_p} \frac{\tilde{\tau}_r}{\sqrt{\tilde{\tau}_r^2 + \tilde{\tau}_\theta^2 + \tilde{\tau}_z^2}} H \left(\frac{\tilde{\sigma}_{\text{eff}}}{\tilde{\sigma}_f} \right), \quad (52)$$

$$\frac{\partial \lambda_\theta}{\partial \tilde{t}} = \sqrt{\frac{3}{2}} \lambda_\theta \dot{d}_0 \frac{R_0^2}{D_0} \left(\frac{\tilde{\sigma}_{\text{eff}}}{\tilde{\sigma}_f} - 1 \right)^{m_p} \frac{\tilde{\tau}_\theta}{\sqrt{\tilde{\tau}_r^2 + \tilde{\tau}_\theta^2 + \tilde{\tau}_z^2}} H \left(\frac{\tilde{\sigma}_{\text{eff}}}{\tilde{\sigma}_f} \right). \quad (53)$$

The strains are related to the displacement as

$$E_r^e = \frac{1}{2} \left[(F_r^e)^2 - 1 \right] = \frac{1}{2} (J^c)^{-2/3} \frac{(1 + \partial \tilde{u} / \partial \tilde{r})^2}{\lambda_r^2} - \frac{1}{2}, \quad (54a)$$

$$E_\theta^e = \frac{1}{2} \left[(F_\theta^e)^2 - 1 \right] = \frac{1}{2} (J^c)^{-2/3} \frac{(1 + \tilde{u} / \tilde{r})^2}{\lambda_\theta^2} - \frac{1}{2}, \quad (54b)$$

$$E_z^e = \frac{1}{2} \left[(F_z^e)^2 - 1 \right] = \frac{1}{2} (J^c)^{-2/3} \frac{(1 + \partial \tilde{w} / \partial \tilde{z})^2}{\lambda_z^2} - \frac{1}{2}. \quad (54c)$$

The Piola-Kirchhoff stresses in Eq. (51) can be expressed in terms of the strains as

$$\tilde{\sigma}_r^0 = J^c \frac{\tilde{Y}(c, \chi_s)}{(1+\nu)(1-2\nu)} [(1-\nu)E_r^e + \nu(E_\theta^e + E_z^e)] \times \frac{2E_r^e + 1}{1 + \partial \tilde{u} / \partial \tilde{r}}, \quad (55a)$$

$$\tilde{\sigma}_\theta^0 = J^c \frac{\tilde{Y}(c, \chi_s)}{(1+\nu)(1-2\nu)} [(1-\nu)E_\theta^e + \nu(E_r^e + E_z^e)] \times \frac{2E_\theta^e + 1}{1 + \tilde{u} / \tilde{r}}, \quad (55b)$$

$$\tilde{\sigma}_z^0 = J^c \frac{\tilde{Y}(c, \chi_s)}{(1+\nu)(1-2\nu)} [(1-\nu)E_z^e + \nu(E_r^e + E_\theta^e)] \times \frac{2E_z^e + 1}{1 + \partial \tilde{w} / \partial \tilde{z}}. \quad (55c)$$

Thus, we can express the Piola-Kirchhoff stresses in terms of the displacement field by substituting Eq. (54) in Eq. (55). The non-dimensional flux in Eq. (50) can be expressed as

$$\tilde{J}_r = -\tilde{D}c \frac{\partial \tilde{\mu}}{\partial \tilde{r}}, \quad (56)$$

where

$$\tilde{\mu} = \frac{\mu_0^0}{R_0 T} + \log(\gamma c) + \mu_{S1}^{\sim} + \mu_{S2}^{\sim} + \mu_{S3}^{\sim} \quad (57)$$

and

$$\tilde{\mu}_{S1}^{\sim} = -\frac{1}{6x_{\text{max}}} \frac{\partial J^c}{\partial c} \frac{\tilde{Y}}{(1+\nu)(1-2\nu)} \times \left[(1-\nu) \left\{ (E_r^e)^2 + (E_\theta^e)^2 + (E_z^e)^2 \right\} \right. \quad (58a)$$

$$\left. + 2\nu(E_r^e E_\theta^e + E_\theta^e E_z^e + E_z^e E_r^e) \right],$$

$$\tilde{\mu}_{S2}^{\sim} = -\frac{1}{3x_{\text{max}}} \frac{\partial J^c}{\partial c} \frac{\tilde{Y}}{(1+\nu)(1-2\nu)} [(1+\nu)(E_r^e + E_\theta^e + E_z^e)],$$

$$\tilde{\mu}_{S3}^{\sim} = \frac{1}{2x_{\text{max}}} J^c \left[\frac{\partial}{\partial c} \left\{ \frac{\tilde{Y}(1-\nu)}{(1+\nu)(1-2\nu)} \right\} \left\{ (E_r^e)^2 + (E_\theta^e)^2 + (E_z^e)^2 \right\} \right. \quad (58b)$$

$$\left. + 2 \frac{\partial}{\partial c} \left\{ \frac{\tilde{Y}\nu}{(1+\nu)(1-2\nu)} \right\} (E_r^e E_\theta^e + E_\theta^e E_z^e + E_z^e E_r^e) \right]. \quad (58c)$$

The non-dimensionalized deviatoric parts of the Cauchy stress tensor in Eqs. (52) and (53) can be further broken down as

$$\tilde{\tau}_{r,\theta,z} = \tilde{\sigma}_{r,\theta,z} = -\frac{1}{3} (\tilde{\sigma}_r + \tilde{\sigma}_\theta + \tilde{\sigma}_z), \quad (59)$$

where

$$\tilde{\sigma}_r = \frac{\tilde{Y}(c, \chi_s)}{(1+\nu)(1-2\nu)} [(1-\nu)E_r^e + \nu(E_\theta^e + E_z^e)] \frac{\sqrt{2E_r^e + 1}}{\sqrt{2E_\theta^e + 1} \sqrt{2E_z^e + 1}}, \quad (60a)$$

$$\tilde{\sigma}_\theta = \frac{\tilde{Y}(c, \chi_s)}{(1+\nu)(1-2\nu)} [(1-\nu)E_\theta^e + \nu(E_r^e + E_z^e)] \frac{\sqrt{2E_\theta^e + 1}}{\sqrt{2E_r^e + 1} \sqrt{2E_z^e + 1}}, \quad (60b)$$

$$\tilde{\sigma}_z = \frac{\tilde{Y}(c, \chi_s)}{(1+\nu)(1-2\nu)} [(1-\nu)E_z^e + \nu(E_r^e + E_\theta^e)] \frac{\sqrt{2E_z^e + 1}}{\sqrt{2E_r^e + 1} \sqrt{2E_\theta^e + 1}}. \quad (60c)$$

Therefore, the non-dimensional effective stress in Eqs. (52) and (53) can be expressed as

$$\tilde{\sigma}_{\text{eff}} = \sqrt{\frac{3}{2}} \sqrt{\tilde{\tau}_r^2 + \tilde{\tau}_\theta^2 + \tilde{\tau}_z^2}. \quad (61)$$

After non-dimensionalization, the initial and boundary conditions corresponding to Eq. (50) can be written as

$$c(\tilde{r}, 0) = 0, \quad \tilde{J}_r(0, \tilde{t}) = 0, \quad \tilde{J}_r(1, \tilde{t}) = \underbrace{\tilde{J}_0(1-c)}_{\text{Charging}} \quad (62)$$

or $\underbrace{-\tilde{J}_0 c}_{\text{Discharging}}.$

The boundary conditions applicable to Eq. (51) are

$$\tilde{u}(0, \tilde{t}) = 0, \quad \tilde{\sigma}_r^0(1, \tilde{t}) = 0. \quad (63)$$

The initial conditions applicable to Eqs. (52) and (53) are

$$\lambda_r(\tilde{r}, 0) = 1 \quad \text{and} \quad \lambda_\theta(\tilde{r}, 0) = 1. \quad (64)$$

When the cylinder is axially constrained, we have no axial strain, $\partial w / \partial z = 0$, whereas when the cylinder is axially unconstrained, there is no axial force,

$$2\pi \int_0^1 \tilde{\sigma}_z^0 r \, dr = 0. \quad (65)$$

Since, $\partial u / \partial r = \partial \tilde{u} / \partial \tilde{r}$,

$$\chi_s = \frac{\tau d_0}{R_0 \left(1 + \frac{\partial \tilde{u}}{\partial \tilde{r}}\right)} \left[\sum_{i \leq 3} C_i \left(C_i^{-(m+3)} - 1 \right) \right]. \quad (66)$$

Here, χ_s is dimensionless.

D. Criteria of buckling

The possibility of buckling arises only for the axially constrained case. When the ends are fixed, the tendency of the cylinder to expand in the axial direction during lithiation gives rise to a compressive axial force. However, if this compressive axial force is larger than a certain critical load, it may lead to buckling of the cylinder. In order to study this, Euler's buckling criteria is chosen which was shown to be valid asymptotically for thin cylinders.⁶⁰ Thus, we have

$$F_{\text{crit}} = \frac{\pi^2 Y I}{(KL)^2}, \quad (67)$$

where F_{crit} is the critical buckling load. Here YI is the flexural rigidity (where Y is the modulus of elasticity and I is the second moment of area), L is the length of beam column and K is a factor which accounts for boundary conditions. We assume here for simplicity that $K = 1$ that corresponds to the physical situation of the column constrained between two frictionless parallel plates.

We consider two modifications of the classical Euler buckling theory following Chakraborty *et al.*,²⁶ additionally, we incorporate another modification due to the incorporation of the BOLS effect. For the first modification, since the radius used for the calculation of the second moment of area is changing with time, we have

$$R = R_0 \left(1 + \frac{\partial u}{\partial r} \right). \quad (68)$$

This modifies the classical Euler buckling criterion because the second moment of area, I , which is a function of radius, changes with time. The second moment of area is given by

$$I = \frac{\pi R^4}{4}. \quad (69)$$

This will be referred to as the first refinement of the Euler Buckling criterion in our further discussions. Now, the Young's modulus of elasticity, Y , is a function of Li concentration and size effect χ_s . Hence, we have a flexural rigidity which varies with position since it is dependent on the modulus of elasticity which varies spatially. We know that the root of flexural rigidity is an integration of the bending stresses over the column cross-section. Here, σ_z is the bending stress. We note that $\sigma_z = \kappa Y r$, where κ is the local curvature of the column.⁶¹ Thus, the moment can be calculated as

$$M = \int_{-R}^R \tilde{r} \sigma_z \, dA, \quad (70)$$

where \tilde{r} is the radial coordinate in the current frame of reference, the elemental area, $dA = 2\sqrt{R^2 - \tilde{r}^2} d\tilde{r}$, and the integration is done throughout the cross-section of the cylindrical anode. Thus, we have the time-dependent flexural rigidity as

$$YI(c, t) = 4 \int_0^R \tilde{r} Y \sqrt{R^2 - \tilde{r}^2} \, d\tilde{r} \quad (71)$$

$$= 4R^4 \int_0^1 \tilde{r}^2 Y_0 (1 + \chi_s) (1 + \eta_E x_{\text{max}} c) \sqrt{1 - \tilde{r}^2} \, d\tilde{r}. \quad (72)$$

We will refer to the modifications related to incorporating the changing Li concentration and the size effect as the second and third refinements of the Euler's buckling criterion, respectively.

It is important to note that accounting for the presence of constraints around the curved surface of the cylindrical electrode particle will entail major changes. The buckling criterion itself would have to be changed because the Euler buckling criterion (even with the aforementioned modifications) will no longer be appropriate. It may be surmised from physical considerations that the presence of such constraints would make the cylinder safer against buckling because these constraints would impart an effective stiffening influence. However, the additional influence of the BOLS effect can only be properly understood through a separate, dedicated study.

III. RESULTS AND DISCUSSIONS

A. Axially unconstrained

Figure 1 shows the variation of Cauchy stresses $\sigma = \text{diag}(\sigma_r, \sigma_\theta, \sigma_z)$ corresponding to three different non-dimensional times (\tilde{t}) for an initial cylinder radius $R_0 = 5$ nm and lithiation rate $\dot{j}_0 = 0.1$ for two cases: (i) with the BOLS effect (χ_s) and (ii) without the BOLS effect ($\chi_s = 0$). The domain of interest is the radius of the unconstrained cylinder. In the work by Chakraborty *et al.*,²⁶ the initial radius of the silicon cylindrical nano-electrode particle was considered to be $R_0 = 200$ nm. However, in our present study, we have focused on the range $5 \text{ nm} \leq R_0 < 30 \text{ nm}$ in order to

highlight the BOLS effect. The reason is that for a particle of nanometre length scale, the surface curvature and the percentage of the surface atoms decrease with increasing particle size, reducing the effect of coordination number imperfection.³² Accordingly, it is found that as we go beyond an initial radius of $R_0 = 30$ nm, the BOLS effect on the stresses is nullified, rendering both the curves (with χ_s vs. without χ_s) for $\{\sigma_r, \sigma_\theta, \sigma_z\}$ indistinguishable from each other.

At a relatively high influx rate of $\dot{j}_0 = 0.1$, when intercalation begins, there is a thin region near the periphery where the lithium concentration quickly increases. Due to the higher volumetric expansion at the surface compared to the bulk, the regions away from the surface experience tensile

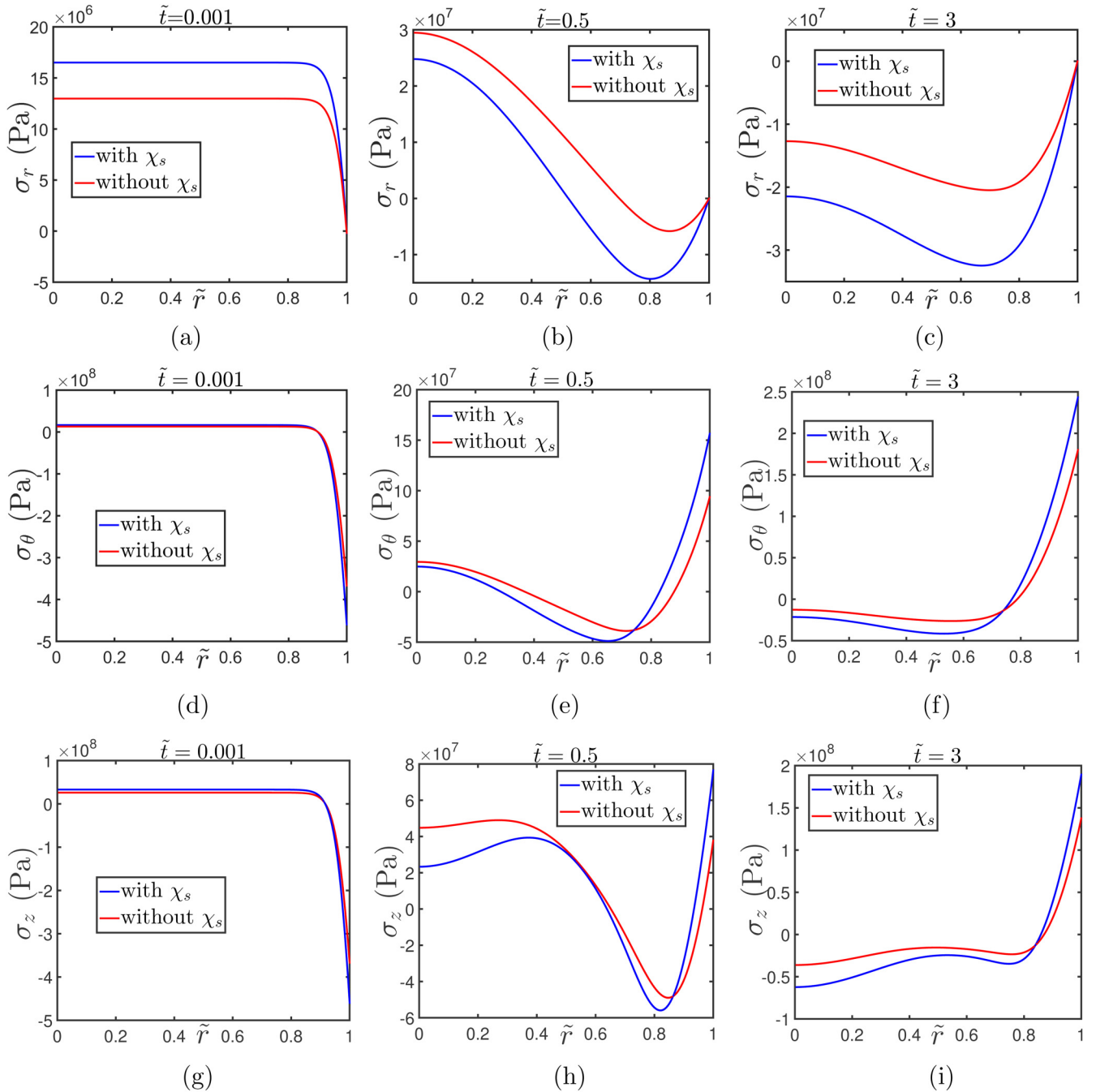


FIG. 1. $\sigma_r, \sigma_\theta, \sigma_z$ for $\dot{j}_0 = 0.1$ for $R_0 = 5$ nm when the cylinder is axially unconstrained.

stresses in the circumferential as well as radial directions as shown in Figs. 1(a) and 1(d). Since there is no traction at the surface, there is no restriction on volumetric expansion in the radial direction and a tensile radial stress is generated just under the surface [see Fig. 1(a)] which is the result of the outward pull of the material points on the material in the bulk and this effect is transferred along the radial direction up to the centre.

In a pristine un lithiated state, due to coordination number imperfection, the bonds of the surface atoms (up to three atomic layer beneath the surface) are shorter and stronger than the bonds of atoms in the bulk initially.³² As we can

see from Fig. 1(a), there is a huge difference in radial stresses at $\tilde{t} = 0.001$ between the two cases (with χ_s vs. without χ_s). The tensile radial stress is significantly more for the case in which we take into account the BOLS effect. When lithiation occurs at the relative high rate of $\tilde{j}_0 = 0.1$, a high number of Si-Si bonds get broken at the surface. The BOLS effect predicts that this bond-breakage gives rise to bond-contraction in the atomic layers close to the surface and thus compensating adjustments to other layer spacing takes place which extends several layers into the solid. Thus, contraction in the surface atomic layers causes a stronger outward pull which gives rise to a higher positive value of σ_r during initial times

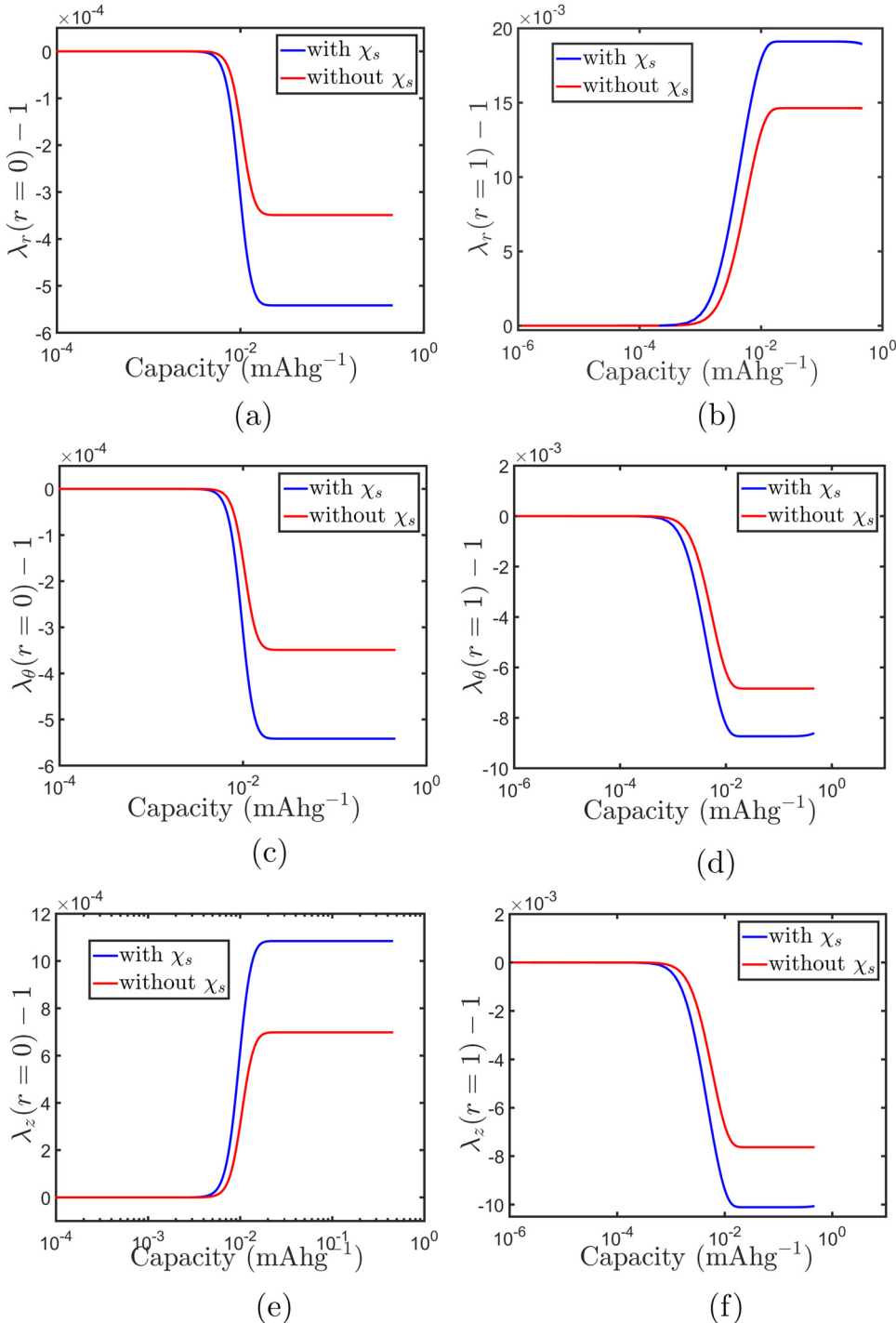


FIG. 2. The plastic stretches for $\tilde{j}_0 = 0.1$ for $R_0 = 5$ nm when the cylinder is axially unconstrained.

for the case with non-zero χ_s . In the axial and azimuthal directions, adjacent material points present a constraint to free movement under lithiation and hence compressive stresses at initial times are induced in those directions, as is clear from Figs. 1(d) and 1(g). However, the compressive stress at the surface is more negative when we consider the size effect. Surface atoms have a shorter bond length due to the BOLS effect and when we try to insert lithium, the compressive stress build-up is more.

At later times, further lithiation leads to an increase in the concentration of Li atoms and more breaking of Si-Si bonds in the bulk. Also, according to the BOLS effect, breaking of one bond leads to neighbouring ones becoming shorter and stiffer. Thus, further insertion of lithium atoms leads to more compressive stress build-up. It can be observed from Fig. 1(b) that at time $\tilde{t} = 0.5$, for the curve in which the BOLS effect is considered, σ_r is less (more negative at points where the stress is compressive and less positive where the stress is tensile) than the curve in which the BOLS effect is not considered. We can also observe that the reversal of radial stress from tensile to compressive occurs at an earlier time if we consider the BOLS effect. At later times also, the compressive stress is more for the case in which the BOLS effect is considered due to further insertion of lithium atoms.

So, as time progresses, lithium atoms diffuse further into the cylinder, and the nature of stresses changes significantly.

We notice that incorporating the BOLS effect predicts a faster transition from tensile to compressive stress because the Young's modulus (Y) is higher due to the $(1 + \chi_s)$ factor [as shown in Fig. 6(b) inset later]. For a given deformation, for higher E , there will be higher $\{\sigma_r, \sigma_\theta, \sigma_z\}$ for both tensile and compressive stresses. We notice from Figs. 1(d)–1(i) that the BOLS effect induces significant changes in the magnitude of the stress at the surface.

Additionally, by studying the Cauchy stresses for $\tilde{j}_0 = 0.001$, we found that σ_r is always tensile and evolution of stress is much slower than that for $\tilde{j}_0 = 0.1$. Even after $\tilde{t} = 300$ (which is approximately equal to a time of 33 h), the radial stress is still tensile in nature throughout the domain (except at the surface, where $\sigma_r = 0$). Initially, there is significant difference in the magnitude of stresses for the two cases (with χ_s vs. without χ_s). However, with time, the BOLS effect is reduced to a proportion such that it is practically negligible for $\tilde{t} > 300$. We also noticed that the effect of BOLS on radial stress is significantly less for $\tilde{j}_0 = 0.001$ than for $\tilde{j}_0 = 0.1$ and in the axial and azimuthal direction, the BOLS effect for $\tilde{j}_0 = 0.001$ is practically negligible for later times. Due to these negligible differences, we do not show the plots. The relatively higher difference between the two cases (with χ_s vs. without χ_s) for a higher influx rate is because a higher rate ensure more bond relaxation per unit time as the BOLS effect is instantaneous.⁶²

Figure 2 depicts the change in plastic stretches at the centre ($\tilde{r} = 0$) and at the periphery ($\tilde{r} = 1$) of the nano-electrode particle for an initial radius of $R_0 = 5$ nm and a lithiation rate of $\tilde{j}_0 = 0.1$ as the lithium concentration increases in the axially unconstrained case. This concentration is represented dimensionally in terms of capacity = $(\int_0^{R_0} c \cdot 2\pi r dr) / (\int_0^{R_0} 2\pi r dr)$ having units of mAhg⁻¹. That

plastic stretches deviate from 1, even at $\tilde{r} = 0$ for a high lithiation rate of $\tilde{j}_0 = 0.1$ was discussed by Chakraborty *et al.*²⁶ We observe that in each case of Fig. 2, for the same capacity level (meaning, effectively, the same level of lithiation), the magnitude of the plastic stretches considering the BOLS effect is higher than that without the BOLS effect. In order to interpret the differences in the plastic stretches corresponding to same values of capacity, we need to discuss stretches, elastic stresses, and lithiation levels together. When silicon is lithiated, the concentration of lithium varies along the radial direction. This heterogeneity of lithium concentration leads to different levels of volume expansion at different radial points. The elastic deformations are induced to maintain the kinematic compatibility despite the tendency of radial points to deform to different extents.⁴⁰ The elastic stresses that accompany these elastic deformations are directly related to the Young's modulus. When the BOLS effect is considered, the value of the Young's modulus is higher. Therefore, for the same level of lithiation, when the BOLS effect is considered, the stresses are higher compared to the case when the BOLS effect is not considered. As a result of the higher stresses, the yield stress value is crossed at slightly lower values of capacity when the BOLS effect is considered. Once the yield stress value is crossed, plastic stretches are manifested (meaning that their values show deviation from 1). The onset of plastic stretches at slightly lower values of capacity with the BOLS effect results in perceptibly higher magnitudes of plastic stretch values for higher values of capacity as seen in Fig. 2.

B. Axially constrained

Figure 3 shows the variation of Cauchy stresses over the radius of the cylinder when the cylinder is axially constrained for different times (\tilde{t}). There is a major difference in stress development between the axially constrained case and unconstrained one. As shown in Fig. 3(b), we can observe that at the axis, radial compressive stresses show up earlier (at $\tilde{t} = 0.5$) than it occurs for the axially unconstrained case (between $1 < \tilde{t} < 2$) as shown in Figs. 1(b) and 1(c). This is due to the constraint in the axial direction which forces all the volumetric expansion (due to lithiation) to occur in the radial and azimuthal direction. This is also the cause of higher increase of stress along both these directions [comparing Figs. 1(a), 1(b), and 1(c) with Figs. 3(a), 3(b), and 3(c) and also comparing Figs. 1(d), 1(e), and 1(f) with Figs. 3(d), 3(e), and 3(f)]. Furthermore, we observe from Fig. 3(a) to 3(c) that the significance of the BOLS effect can only be observed during initial times. Unlike its unconstrained counterpart, the BOLS effect on radial stress for an axially constrained cylinder is negligible at later times. From Figs. 3(d)–3(i), we observe that the BOLS effect has no significant effect on either axial or azimuthal stress. The curves for the two cases (with χ_s vs. without χ_s) practically overlap on each other after time $\tilde{t} = 1$ for both the stresses.

However, from Fig. 3, we note that for the axially constrained case, the BOLS effect is more for $\tilde{j}_0 = 0.1$ than for $\tilde{j}_0 = 0.001$ (plots for $\tilde{j}_0 = 0.001$ are not shown). As discussed earlier in Sec. III A, since the BOLS effect is

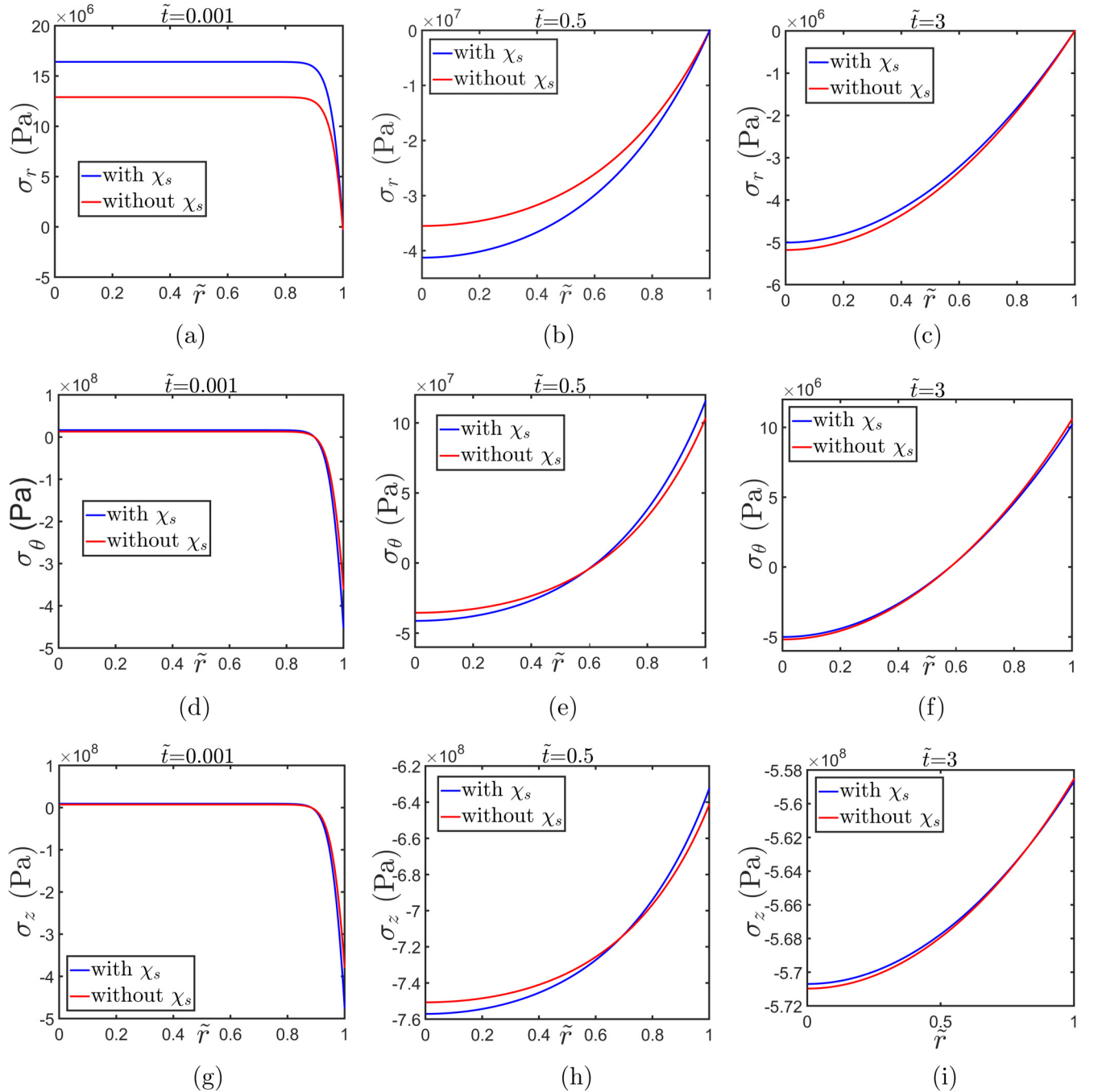


FIG. 3. σ_r , σ_θ , σ_z for $\tilde{j}_0 = 0.1$ for $R_0 = 5$ nm when the cylinder is axially constrained.

instantaneous,⁶² a higher lithiation rate ensures more bond relaxation per unit time and hence the BOLS effect is more for a higher lithiation rate.

Figure 4 shows the variation of plastic stretches at the surface ($\tilde{r} = 1$) and at the axis ($\tilde{r} = 0$) for an initial radius of $R_0 = 5$ nm and lithiation rate of $\tilde{j}_0 = 0.1$ as the lithium concentration increases in the axially constrained electrode. We observe that the plastic stretches deviate from a value of 1 at the centre for $\tilde{j}_0 = 0.1$ [see Figs. 4(a)–4(f)] and in our studies, we have found that it does so for $\tilde{j}_0 = 0.001$ also (for the axially constrained case). This observation is in clear contrast to that for the unconstrained case, where for $\tilde{j}_0 = 0.001$, the plastic stretches do not deviate from a value

of 1 even after a time of $\tilde{t} = 300$. As previously mentioned plots for $\tilde{j}_0 = 0.001$ are not shown.

For $\tilde{j}_0 = 0.001$, the plots for the two cases (with χ_s vs. without χ_s) practically overlap for both axially constrained and unconstrained situations. So we note that for a relatively low influx rate of $\tilde{j}_0 = 0.001$ which is comparable to the relaxation time of lithium diffusion, the BOLS effect is negligible on the plastic stretches although it has significant effect on the Cauchy stress at those low rates. We note that the BOLS effect for axially constrained case is far less than that for the axially unconstrained case and so the trends observed are quite similar for the two cases (with χ_s vs. without χ_s) with minute differences in magnitude. For $\tilde{j}_0 = 0.1$, at the

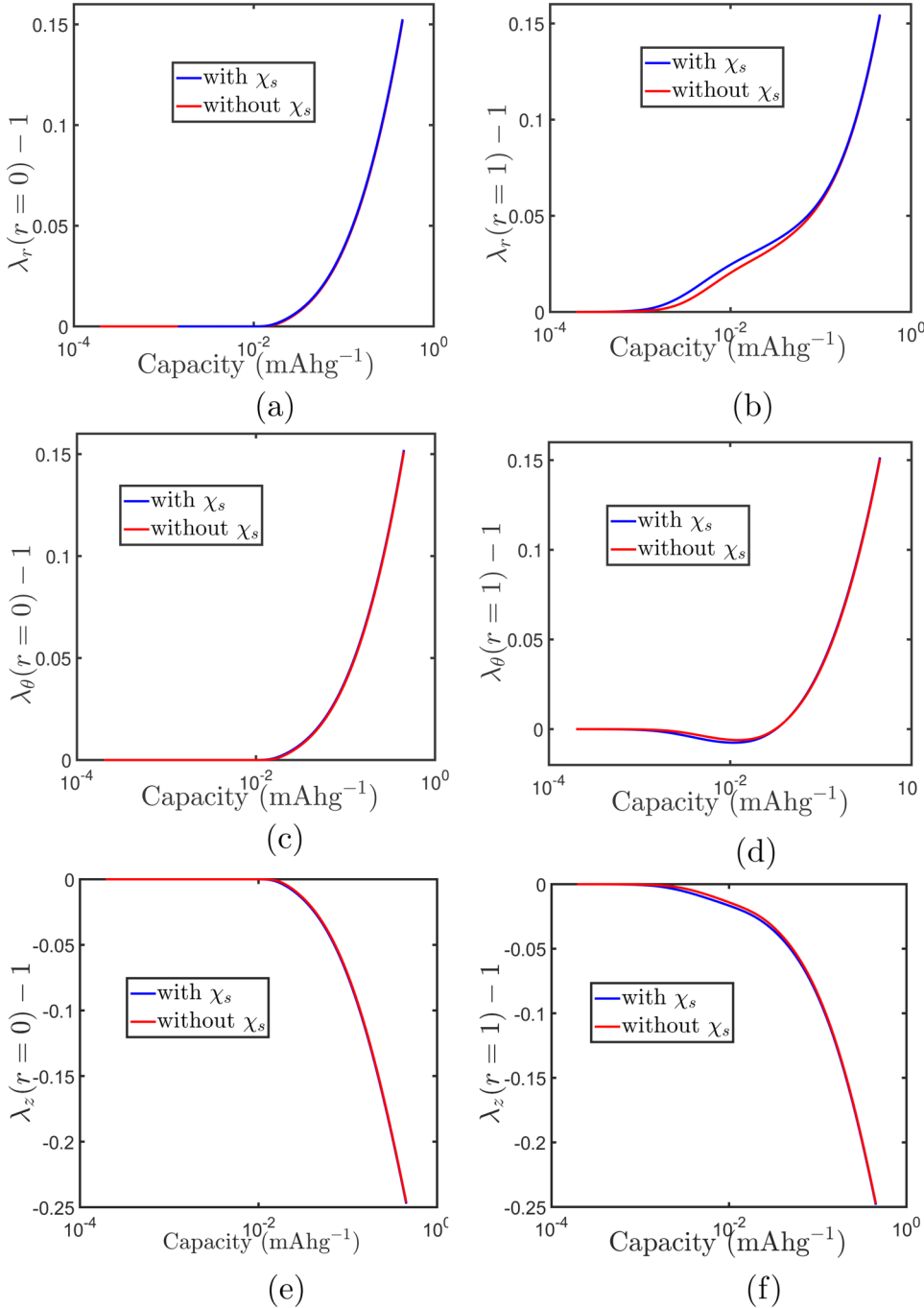


FIG. 4. The plastic stretches for $\tilde{j}_0 = 0.1$ for $R_0 = 5$ nm when the cylinder is axially constrained.

surface, the BOLS effect causes the radial plastic stretch to deviate more from the value of 1 at a capacity of 0.01 mAh g^{-1} for $R_0 = 5$ nm and also for $R_0 = 10$ nm (plots for $R_0 = 10$ nm not shown).

As shown in Fig. 4(d), the azimuthal plastic stretch at the surface at a high influx rate of $\tilde{j}_0 = 0.1$ for $R_0 = 5$ nm decreases to a value less than 1, and then as the concentration increases, the plastic stretch increases to a value greater than 1. Therefore, for a high influx rate, the surface first undergoes a compressive plastic yielding in the azimuthal direction and then a reversal to tensile plastic yielding. This trend of reversal of azimuthal plastic stretch is also observed for $R_0 = 10$ nm and in the works of Chakraborty *et al.*²⁶ for a radius of $R_0 = 200$ nm.

We have studied the development of $\{\sigma_r, \sigma_\theta, \sigma_z\}$ with time over the radius of the cylinder for an initial radius $R_0 = 5$ nm, 10 nm, 20 nm, 30 nm. We observe that the difference between the curves for the two cases (with χ_s vs. without χ_s) reduces as we increase the radius of the cylinder. In fact, for $R_0 > 10$ nm, in the azimuthal and axial directions, the curves overlap to a great extent. This is expected because the BOLS effect reduces as the specimen size increases.

C. Buckling

We discuss the role of the axial force, the BOLS effect, and the changing concentration on the buckling of the cylinder. In Fig. 5(a), we show the time-variant critical axial load

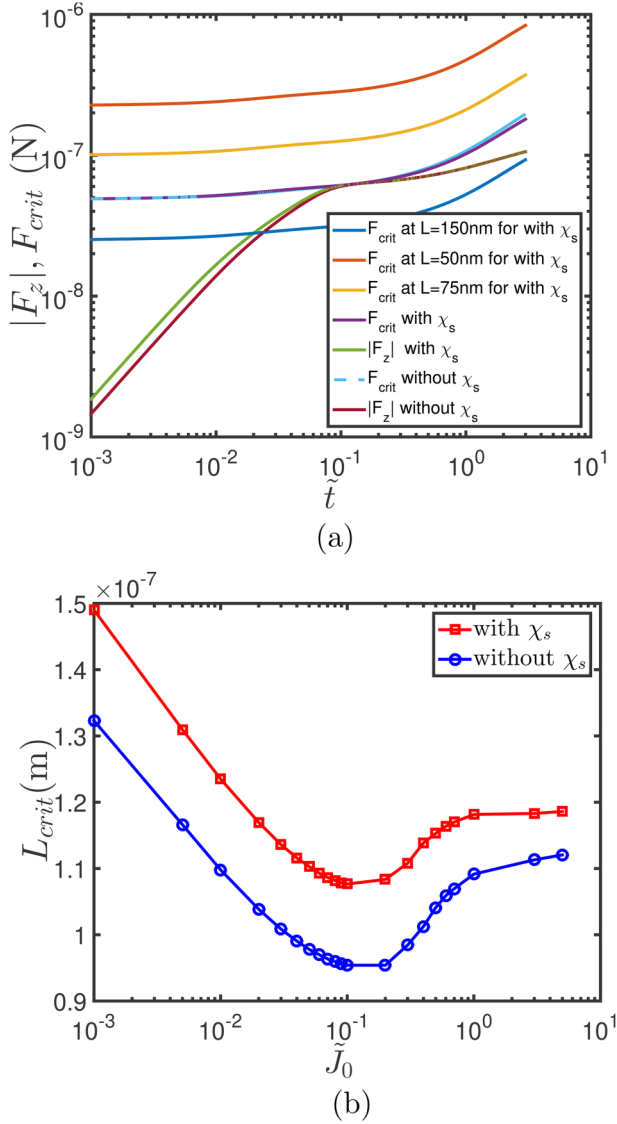


FIG. 5. Panel (a) shows the time variant load lines for different lengths of the cylinder for $R_0 = 5$ nm and influx rate $\tilde{j}_0 = 0.1$ along with the critical load lines for both the cases (with χ_s vs without χ_s) along with the plot of the corresponding axial forces for both with χ_s and without χ_s conditions. Panel (b) shows the critical length of buckling for various \tilde{j}_0 .

for buckling F_{crit} for different cylinder lengths L for $R_0 = 5$ nm and influx rate $\tilde{j}_0 = 0.1$ taking into account the BOLS effect. We also show the axial force F_z as a function of time for both the cases (with χ_s vs without χ_s). For a particular length of the cylinder, the intersection of the corresponding critical axial load line and the axial force curve provides the time at which the buckling will occur under the mentioned conditions. We notice that there exists a particular load line corresponding to critical length L_{crit} which just touches the axial force curve. If we further decrease the length of the cylinder even by an infinitesimal amount, the cylinder will never buckle. This special condition occurs due to the influence of the time-variant radius and will never occur for the case of the classical Euler buckling criterion. If radius were constant, the critical axial load line for a particular cylinder length and the axial force would be two horizontal lines and hence no critical value of length could be found in that case unless the two lines were coincident.

It is important to note from Fig. 5(a) that the axial forces F_z for the two cases (with χ_s and without χ_s) for \tilde{j}_0 converges approximately at $\tilde{t} = 0.1$ (before the critical load lines touches the corresponding F_z curves). The value of F_{crit} is also approximately same for the two cases but still the critical length of buckling is different for the two cases. This can be explained by the fact that the BOLS effect increases the Young's modulus making the cylinder stiffer; hence, a higher critical length L_{crit} is needed to reach a load line that will be tangential to the axial force load line.

In Fig. 5(b), we show the critical buckling length (L_{crit}) vs lithiation rate \tilde{j}_0 for a radius of $R_0 = 5$ nm. We observe that both the curves in Fig. 5(b) has much higher L_{crit} for a very low rate of lithiation $\tilde{j}_0 = 0.001$ and for a very high lithiation rate of $\tilde{j}_0 = 1$ as compared to the L_{crit} for a moderate lithiation rate of $\tilde{j}_0 = 0.1$. The same has been observed by Chakraborty *et al.*²⁶ (of course, they considered a cylindrical radius of $R_0 = 200$ nm and hence did not include the BOLS effect). We also note that the curve for the case in which the BOLS effect is considered lies above the curve in which the BOLS effect is not considered. However, the curve in which the BOLS effect is considered qualitatively looks like a scaled up version of the other curve up to a moderate value of $\tilde{j}_0 = 0.2$. After $\tilde{j}_0 = 0.2$, the gap between the two curves starts reducing. This is to be expected because of the fact that as lithiation rate \tilde{j}_0 increases, the radius also increases significantly within a very short period of time and hence, the BOLS effect is reduced. We also observe that for a lithiation rate of $\tilde{j}_0 = 1$ or above, the slope of both curves in Fig. 5(b) reduces drastically. This reduction in slope is not observed if we take a constant Young's modulus Y , a trend that was observed in Fig. 6(b) of the paper by Chakraborty *et al.*²⁶

In Fig. 6(a), we show the variation of the percentage increase in L_{crit} ($\% \Delta L_{crit}$) due to the BOLS effect with increasing initial radius of the cylinder (R_0) for an influx rate of $\tilde{j}_0 = 0.1$ and 0.001 . We observe that as we increase R_0 , the percentage increase in L_{crit} reduces drastically which is expected since the BOLS effect is prominent at lower values of R_0 . For an influx rate of $\tilde{j}_0 = 0.1$, for $R_0 = 2.5$ nm, $\% \Delta L_{crit} = 27$ and for $R_0 = 100$ nm, $\% \Delta L_{crit} = 0.6$. In fact, the value of $\% \Delta L_{crit}$ decreases to a value less than 2 at $R_0 = 30$ nm. As we already discussed in Subsection III A, the BOLS effect has significant influence on the stresses when we consider an initial radius R_0 less than 30 nm. We can observe that the curves for $\tilde{j}_0 = 0.1$ and 0.001 practically overlap and that they approximately follow the equation

$$\% \Delta L_{crit} = 100(e^{\frac{1}{1.72R_0}} - 1). \quad (73)$$

In Fig. 6(b), we show percentage increase of the Young's modulus (ΔY) between the two cases (with χ_s and without χ_s) vs the initial radius R_0 of the cylinder for an influx rate, $\tilde{j}_0 = 0.1$ at the surface of the cylinder for three instants of non-dimensional time, \tilde{t} . We observe that the effect of BOLS on ΔY is highest at lower values of radius. We can also observe from the inset of Fig. 6(b) that the difference is larger at initial times than at later times due to increase in radius and consequent decrease in the BOLS effect. It is to be noted that the variation of ΔY as well as Y with time is

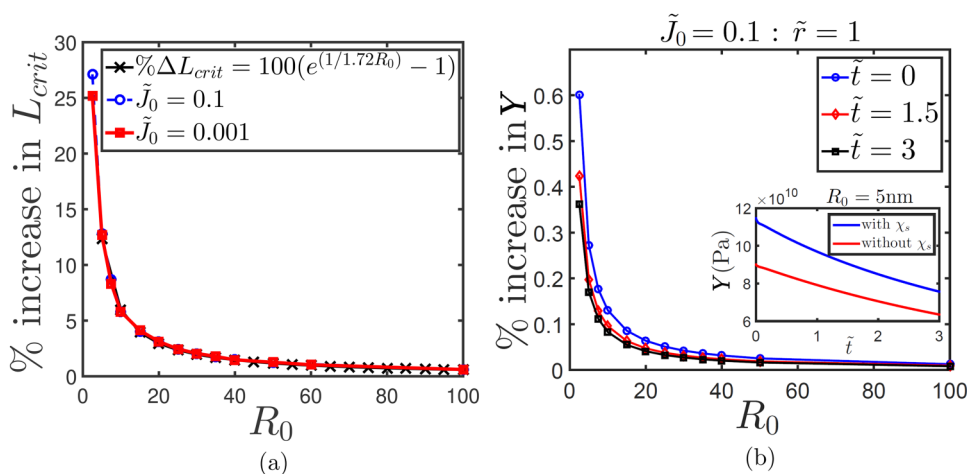


FIG. 6. Panel (a) shows the percentage increase in the critical length of buckling L_{crit} due to the consideration of the BOLS effect for $\tilde{J}_0 = 0.1$ and 0.001 for various initial radii R_0 . Panel (b) shows the percentage increase in Y for various values of R_0 for $\tilde{J}_0 = 0.1$ and $\tilde{r} = 1$.

significantly higher for lower values of initial radius, R_0 . We have observed that the variation of ΔY with R_0 is almost independent of location, i.e., the curves are almost same whether we consider the Young's modulus at the centre or at the surface. We have also observed that the curves are same for both axially constrained and unconstrained cases.

IV. CONCLUSIONS

We have performed a detailed analysis of the changes induced by the BOLS effect in a silicon cylindrical nanoelectrode particle. We have noticed that there are certain differences in stress distribution as well as plastic stretch distribution when the BOLS effect is considered. In almost all the cases studied, stresses and plastic stretches are amplified in magnitude. We have also observed that the reversal from tensile to compressive stresses occurs earlier when we consider the BOLS effect. It has also been observed that the BOLS effect reduces as we increase the radius of the cylinder. We have found that a smaller electrode radius to small values gives a higher critical length of buckling than usual (as found from the Euler buckling criteria). Although the critical length ΔL_{crit} increases steadily with increasing R_0 , the percentage increase in L_{crit} due to the BOLS effect reduces significantly with increasing R_0 .

The focus of our current investigation has been on the effects of the BOLS theory on buckling of a specimen that is geometrically a canonical instance of the classical Euler buckling case. However, the importance of this investigation must be understood by placing it in the more general context of mechanical instability. Within this broader context, phenomena involving delamination (peeling, blistering) of two layers of materials are particularly relevant in studies of lithium-ion batteries because of the presence of layered structures within these batteries; for instance, delamination of an active material like Si from a current collector like Cu. Since mechanical instability of such structures is intrinsically dependent on interfacial properties, considerations of the BOLS theory become tremendously pertinent. Important progress was recently made toward the fundamental understanding of such interfacial properties with particular relevance to delamination using

the BOLS theory.⁶³ It is to be expected that an exciting direction of future investigations will be toward incorporating the BOLS theory within mathematical frameworks for studying a broader category of mechanical instability issues in lithium-ion batteries, and thus contribute to the advancement of this technology in a fundamental way.

ACKNOWLEDGMENTS

S.N. and J.C. thank Professor Colin Please and Professor Jon Chapman (University of Oxford) for a critical reading of the manuscript; J.C. additionally thanks Professor Alain Goriely (also at University of Oxford) for earlier discussions. J.C. thanks the DST-INSPIRE program of the Government of India (DST/INSPIRE Faculty Award/2016/DST/INSPIRE/04/2015/002825) as well as the ISIRD Funding (IIT/SRIC/ME/MFD/2017-18/70) from IIT Kharagpur for the computational resources.

¹J.-M. Tarascon and M. Armand, "Issues and challenges facing rechargeable lithium batteries," *Nature* **414**, 359–367 (2001).

²E. Gladyshevskii, G. Olekshiv, and P. Kripyakevich, "New examples of the structural type $\text{Li}_{22}\text{Pb}_5$," *Kristallografiya* **9**, 338–341 (1964).

³A. Mauger and C. M. Julien, "Nanoscience supporting the research on the negative electrodes of Li-ion batteries," *Nanomaterials* **5**, 2279–2301 (2015).

⁴T. H. Hwang, Y. M. Lee, B.-S. Kong, J.-S. Seo, and J. W. Choi, "Electrospun core-shell fibers for robust silicon nanoparticle-based lithium ion battery anodes," *Nano Lett.* **12**, 802–807 (2012).

⁵U. Maver, A. Žnidaršič, and M. Gaberšček, "An attempt to use atomic force microscopy for determination of bond type in lithium battery electrodes," *J. Mater. Chem.* **21**, 4071–4075 (2011).

⁶S. K. Soni, B. W. Sheldon, X. Xiao, M. W. Verbrugge, A. Dongjoo, H. Hafitbaradaran, and G. Huajian, "Stress mitigation during the lithiation of patterned amorphous Si islands," *J. Electrochem. Soc.* **159**, A38–A43 (2011).

⁷K.-L. Lee, J.-Y. Jung, S.-W. Lee, H.-S. Moon, and J.-W. Park, "Electrochemical characteristics of a-si thin film anode for li-ion rechargeable batteries," *J. Power Sources* **129**, 270–274 (2004).

⁸M. Park, G. Wang, H.-K. Liu, and S. Dou, "Electrochemical properties of si thin film prepared by pulsed laser deposition for lithium ion micro-batteries," *Electrochim. Acta* **51**, 5246–5249 (2006).

⁹P. Raimann, N. Hochgatterer, C. Korepp, K. Möller, M. Winter, H. Schröttner, F. Hofer, and J. Besenhard, "Monitoring dynamics of electrode reactions in li-ion batteries by in situ esem," *Ionics* **12**, 253–255 (2006).

¹⁰U. Kasavajjula, C. Wang, and A. J. Appleby, "Nano- and bulk-silicon-based insertion anodes for lithium-ion secondary cells," *J. Power Sources* **163**, 1003–1039 (2007).

- ¹¹C. K. Chan, H. Peng, G. Liu, K. McIlwrath, X. F. Zhang, R. A. Huggins, and Y. Cui, "High-performance lithium battery anodes using silicon nanowires," *Nat. Nanotechnol.* **3**, 31–35 (2008).
- ¹²M. Ebner, F. Marone, M. Stampanoni, and V. Wood, "Visualization and quantification of electrochemical and mechanical degradation in li ion batteries," *Science* **342**, 716–720 (2013).
- ¹³H. Kim, J. Choi, H.-J. Sohn, and T. Kang, "The insertion mechanism of lithium into Mg₂Si anode material for li-ion batteries," *J. Electrochem. Soc.* **146**, 4401–4405 (1999).
- ¹⁴M. Wachtler, M. Winter, and J. O. Besenhard, "Anodic materials for rechargeable li-batteries," *J. Power Sources* **105**, 151–160 (2002).
- ¹⁵J. W. Kim, J. H. Ryu, K. T. Lee, and S. M. Oh, "Improvement of silicon powder negative electrodes by copper electroless deposition for lithium secondary batteries," *J. Power Sources* **147**, 227–233 (2005).
- ¹⁶M.-H. Park, M. G. Kim, J. Joo, K. Kim, J. Kim, S. Ahn, Y. Cui, and J. Cho, "Silicon nanotube battery anodes," *Nano Lett.* **9**, 3844–3847 (2009).
- ¹⁷T. Song, J. Xia, J.-H. Lee, D. H. Lee, M.-S. Kwon, J.-M. Choi, J. Wu, S. K. Doo, H. Chang, W. I. Park, et al. "Arrays of sealed silicon nanotubes as anodes for lithium ion batteries," *Nano Lett.* **10**, 1710–1716 (2010).
- ¹⁸I. Kovalenko, B. Zdyrko, A. Magasinski, B. Hertzberg, Z. Milicev, R. Burtovyy, I. Luzinov, and G. Yushin, "A major constituent of brown algae for use in high-capacity li-ion batteries," *Science* **334**, 75–79 (2011).
- ¹⁹J. Yang, M. Winter, and J. Besenhard, "Small particle size multiphase li-alloy anodes for lithium-ionbatteries," *Solid State Ionics* **90**, 281–287 (1996).
- ²⁰C. K. Chan, R. N. Patel, M. J. Oconnell, B. A. Korgel, and Y. Cui, "Solution-grown silicon nanowires for lithium-ion battery anodes," *ACS Nano*. **4**, 1443–1450 (2010).
- ²¹J. R. Szczech and S. Jin, "Nanostructured silicon for high capacity lithium battery anodes," *Energy Environ. Sci.* **4**, 56–72 (2011).
- ²²L.-F. Cui, L. Hu, J. W. Choi, and Y. Cui, "Light-weight free-standing carbon nanotube-silicon films for anodes of lithium ion batteries," *ACS Nano*. **4**, 3671–3678 (2010).
- ²³J.-L. Zang, and Y.-P. Zhao, "Silicon nanowire reinforced by single-walled carbon nanotube and its applications to anti-pulverization electrode in lithium ion battery," *Compos. B Eng.* **43**, 76–82 (2012).
- ²⁴K. Ogata, E. Salager, C. Kerr, A. Fraser, C. Ducati, A. Morris, S. Hofmann, and C. Grey, "Revealing lithium-silicide phase transformations in nanostructured silicon-based lithium ion batteries via in situ NMR spectroscopy," *Nat. Commun.* **5**, 3217 (2014).
- ²⁵L. Mai, X. Tian, X. Xu, L. Chang, and L. Xu, "Nanowire electrodes for electrochemical energy storage devices," *Chem. Rev.* **114**, 11828–11862 (2014).
- ²⁶J. Chakraborty, C. P. Please, A. Goriely, and S. J. Chapman, "Combining mechanical and chemical effects in the deformation and failure of a cylindrical electrode particle in a Li-ion battery," *Int. J. Solids Struct.* **54**, 66–81 (2015).
- ²⁷K. Zhang, Y. Li, B. Zheng, G. Wu, J. Wu, and F. Yang, "Large deformation analysis of diffusion-induced buckling of nanowires in lithium-ion batteries," *Int. J. Solids Struct.* **108**, 230–243 (2017).
- ²⁸T. K. Bhandakkar and H. T. Johnson, "Diffusion induced stresses in buckling battery electrodes," *J. Mech. Phys. Solids* **60**, 1103–1121 (2012).
- ²⁹Y.-T. Cheng and M. W. Verbrugge, "The influence of surface mechanics on diffusion induced stresses within spherical nanoparticles," *J. Appl. Phys.* **104**, 083521 (2008).
- ³⁰I. Ryu, J. W. Choi, Y. Cui, and W. D. Nix, "Size-dependent fracture of si nanowire battery anodes," *J. Mech. Phys. Solids* **59**, 1717–1730 (2011).
- ³¹X. H. Liu, L. Zhong, S. Huang, S. X. Mao, T. Zhu, and J. Y. Huang, "Size-dependent fracture of silicon nanoparticles during lithiation," *ACS Nano*. **6**, 1522–1531 (2012).
- ³²C. Q. Sun, B. Tay, X. Zeng, S. Li, T. Chen, J. Zhou, H. Bai, and E. Jiang, "Bond-order–bond-length–bond-strength (bond-ols) correlation mechanism for the shape-and-size dependence of a nanosolid," *J. Phys. Condens. Matter* **14**, 7781 (2002).
- ³³Z. Ma, X. Gao, Y. Wang, and C. Lu, "Effects of size and concentration on diffusion-induced stress in lithium-ion batteries," *J. Appl. Phys.* **120**, 025302 (2016).
- ³⁴V. Vijayaraghavan, A. Garg, and L. Gao, "Fracture mechanics modelling of lithium-ion batteries under pinch torsion test," *Measurement* **114**, 382–389 (2018).
- ³⁵H. Wu, Z. Xie, Y. Wang, C. Lu, and Z. Ma, "Modeling diffusion-induced stress on two-phase lithiation in lithium-ion batteries," *Eur. J. Mech. A Solids* **71**, 320–325 (2018).
- ³⁶B. Hu, Z. Ma, W. Lei, Y. Zou, and C. Lu, "A chemo-mechanical model coupled with thermal effect on the hollow core–shell electrodes in lithium-ion batteries," *Theor. Appl. Mech. Lett.* **7**, 199–206 (2017).
- ³⁷Z. Ma, H. Wu, Y. Wang, Y. Pan, and C. Lu, "An electrochemical-irradiated plasticity model for metallic electrodes in lithium-ion batteries," *Int. J. Plast.* **88**, 188–203 (2017).
- ³⁸Z. Ma, Z. Xie, Y. Wang, and C. Lu, "Softening by electrochemical reaction-induced dislocations in lithium-ion batteries," *Scr. Mater.* **127**, 33–36 (2017).
- ³⁹X. Gao, Z. Ma, W. Jiang, P. Zhang, Y. Wang, Y. Pan, and C. Lu, "Stress–strain relationships of lixsn alloys for lithium ion batteries," *J. Power Sources* **311**, 21–28 (2016).
- ⁴⁰Z. Cui, F. Gao, and J. Qu, "A finite deformation stress-dependent chemical potential and its applications to lithium ion batteries," *J. Mech. Phys. Solids* **60**, 1280–1295 (2012).
- ⁴¹E. H. Lee, *Elastic-plastic Deformation at Finite Strains* (ASME, 1969).
- ⁴²Y. Gao, M. Cho, and M. Zhou, "Mechanical reliability of alloy-based electrode materials for rechargeable Li-ion batteries," *J. Mech. Sci. Technol.* **27**, 1205–1224 (2013).
- ⁴³X. H. Liu, H. Zheng, L. Zhong, S. Huang, K. Karki, L. Q. Zhang, Y. Liu, A. Kushima, W. T. Liang, J. W. Wang et al., "Anisotropic swelling and fracture of silicon nanowires during lithiation," *Nano Lett.* **11**, 3312–3318 (2011).
- ⁴⁴H. Haftbaradaran, J. Song, W. Curtin, and H. Gao, "Continuum and atomistic models of strongly coupled diffusion, stress, and solute concentration," *J. Power Sources* **196**, 361–370 (2011).
- ⁴⁵A. F. Bower, P. R. Guduru, and V. A. Sethuraman, "A finite strain model of stress, diffusion, plastic flow, and electrochemical reactions in a lithium-ion half-cell," *J. Mech. Phys. Solids* **59**, 804–828 (2011).
- ⁴⁶M. Sinnott, *The Solid State for Engineers* (Wiley and Sons, New York, 1963).
- ⁴⁷O. G. Shpyrko, A. Y. Grigoriev, C. Steimer, P. S. Pershan, B. Lin, M. Meron, T. Graber, J. Gerhardt, B. Ocko, and M. Deutsch, "Anomalous layering at the liquid Sn surface," *Phys. Rev. B* **70**, 224206 (2004).
- ⁴⁸H.-E. Mahnke, H. Haas, E. Holub-Krappe, V. Koteski, N. Novakovic, P. Fochuk, and O. Panchuk, "Lattice distortion around impurity atoms as dopants in CdTe," *Thin Solid Films* **480**, 279–282 (2005).
- ⁴⁹Q. Chang, "Theory of size, confinement, and oxidation effects," in *Synthesis, Properties, and Applications of Oxide Nanomaterials* (John Wiley & Sons, 2017), Vol. 9.
- ⁵⁰C. Q. Sun, T. Chen, B. Tay, S. Li, Y. Zhang, H. Huang, L. Pan, S. Lau, and X. Sun, "An extended quantum confinement theory: Surface-coordination imperfection modifies the entire band structure of a nanosolid," *J. Phys. D Appl. Phys.* **34**, 3470 (2001).
- ⁵¹V. M. Goldschmidt, "Krystallbau und chemische Zusammensetzung," *Ber. Dtsch. Chemischen Ges. A and B Ser.* **60**, 1263–1296 (1927).
- ⁵²P. J. Feibelman, "Relaxation of hcp (0001) surfaces: A chemical view," *Phys. Rev. B* **53**, 13740 (1996).
- ⁵³L. Pauling, "Atomic radii and interatomic distances in metals," *J. Am. Chem. Soc.* **69**, 542–553 (1947).
- ⁵⁴W. Huang, R. Sun, J. Tao, L. Menard, R. Nuzzo, and J. Zuo, "Coordination-dependent surface atomic contraction in nanocrystals revealed by coherent diffraction," *Nat. Mater.* **7**, 308–313 (2008).
- ⁵⁵H. Ibach, "The role of surface stress in reconstruction, epitaxial growth and stabilization of mesoscopic structures," *Surf. Sci. Rep.* **29**, 195–263 (1997).
- ⁵⁶W. Haiss, "Surface stress of clean and adsorbate-covered solids," *Rep. Prog. Phys.* **64**, 591 (2001).
- ⁵⁷C. Sun, B. Tay, S. Lau, X. Sun, X. Zeng, S. Li, H. Bai, H. Liu, Z. Liu, and E. Jiang, "Bond contraction and lone pair interaction at nitride surfaces," *J. Appl. Phys.* **90**, 2615–2617 (2001).
- ⁵⁸J. Li, S. Ma, X. Liu, Z. Zhou, and C. Q. Sun, "ZnO meso-mechano-thermo physical chemistry," *Chem. Rev.* **112**, 2833–2852 (2012).
- ⁵⁹Z. Ma, T. Li, Y. Huang, J. Liu, Y. Zhou, and D. Xue, "Critical silicon-anode size for averting lithiation-induced mechanical failure of lithium-ion batteries," *RSC Adv.* **3**, 7398–7402 (2013).
- ⁶⁰R. De Pascalis, M. Destrade, and A. Goriely, "Nonlinear correction to the Euler buckling formula for compressed cylinders with guided-guided end conditions," *J. Elast.* **102**, 191–200 (2011).
- ⁶¹P. Howell, G. Kozyreff, and J. Ockendon, *Applied Solid Mechanics* (Cambridge University Press, 2009), Vol. 43.
- ⁶²C. Q. Sun, "Size dependence of nanostructures: Impact of bond order deficiency," *Prog. Solid State Chem.* **35**, 1–159 (2007).
- ⁶³Y. Wang, Y. Pu, Z. Ma, Y. Pan, and C. Q. Sun, "Interfacial adhesion energy of lithium-ion battery electrodes," *Extreme Mech. Lett.* **9**, 226–236 (2016).